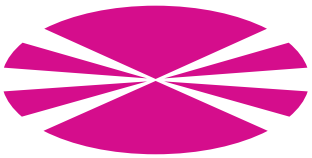

UNIVERSIDADE DA CORUÑA

Escuela Técnica Superior de Ingenieros

de Caminos, Canales y Puertos

Technical Project

A multi-layered in-silico model for rupture risk assessment of abdominal aortic aneurysms with non-atherosclerotic intimal thickening

By

Mario de Lucio Alonso

Supervisors

Jacobo Díaz García

Luis Esteban Romera Rodríguez

2018

A mis padres, Ana y Rafael, que siempre creyeron que llegaría.
Yo aun no he llegado, pero ellos siguen creyendo.

Acknowledgments

Everybody has that person in their life that they admire. Aside from my parents, whenever I think of the person that I admire the most, professionally and personally, even though sometimes it has been tough to deal with him because of his frankness and way of being, I can only think of Miguel Costas. It might be said that Miguel discovered me as a researcher. He has been supervising my work since I started in the field, including this Technical Project and its derived article. Last summer, he gave me the amazing opportunity to work at the structural department of one of the most distinguished universities in the world, the Norwegian University of Science and Technology, where I had the best experience of my life so far, and for which my family and I are extremely grateful. I have never told him, and I do not know whether he will read this or not, but for me he is like the "big brother" that I have never had.

In the same vain, I would like to thank the person who started everything, Marcos Fernández. He not only encouraged me to enrol in the project but also supported me in my down moments. His assistance has been crucial to fulfil the project's ambitions, and I look forward to further collaboration with him in this investigation. I can honestly say that, during this time we have become more than just friends or workmates, and now we are family.

I would like to thank my supervisors, Dr. Jacobo Díaz and Dr. Luis E. Romera, for their extraordinary support, encouragement, and magnificent supervision throughout this difficult project. I will always be thankful for your priceless advice, and for making me feel a valued member of the group.

To Alejandro Soriano, Luis Pire and Javier Paz, for your unconditional friendship and support during this project, specially to Javier Paz for helping me with the post-processing work.

To Marina García López-Arias, for your psychological support and endless affection. Thank you for your patience listening to my unimportant problems, even when you did not understand them, and for being my muse through difficult times.

And last but not least, I would like to express my sincere appreciation to my family, particularly to my parents, who gave me the opportunity to come to Galicia and pursue my dream.

Abstract

An abdominal aortic aneurysm is a localized bulge or swelling in the lower part of the aorta, the main blood vessel of the human body that goes from the left ventricle of the heart down through the chest and the tummy, where it splits in two smaller vessels called iliac arteries. They usually remain asymptomatic until rupture, which makes them a life-threatening disease with an overall mortality of more than 80%. Layer-specific experimental data for human aortic tissue suggest that, in aged arteries and arteries with non-atherosclerotic intimal thickening, the innermost layer of the aorta increases significantly its stiffness and thickness, becoming load-bearing. However, there are very few computational studies of aortic abdominal aneurysms (AAAs) that take into account the mechanical contribution of the three layers that make up the aneurysmal tissue. In this technical project, a three-layered finite element model is proposed from the simplest (uniaxial) stress state, to geometrically parametrized models of AAAs with different asymmetry values. Comparisons are made between a three-layered artery wall, and a mono-layered intact artery, whose constitutive parameters stand for the mean mechanical behavior of the three layers. Likewise, the response of our idealized geometries is compared with similar models. The mechanical contributions of adventitia, media and intima, are also analyzed for the three-layered aneurysms through the evaluation of the mean stress absorption percentage. Results show the relevance of considering the inclusion of tunica intima in multi-layered models of AAAs for getting more accurate results in terms of peak wall stresses and displacements. The last part of this investigation contains a Fluid-Structure Interaction study in parametrized abdominal aortic aneurysms, considering a hyperelastic anisotropic constitutive law for the aneurysmal wall. Because of the high computational cost that it would attain to model a full cardiac cycle in a three-layered aneurysm considering the Fluid-Structure Interaction, only a mono-layered aneurysm is simulated within this final part of the project. As in the previous section, comparisons are made between elastic, hyperelastic isotropic and hyperelastic anisotropic artery walls in terms of stresses and displacements.

Resumen

El aneurisma de la aorta abdominal es un bulto o hinchazón localizada en la parte inferior de la aorta, el principal vaso sanguíneo del cuerpo humano que nace en el ventrículo izquierdo del corazón y viaja a través del pecho y el abdomen hasta llegar a la bifuración iliaca, donde se separa en dos vasos de menor tamaño que reciben el nombre de arterias iliacas. Los aneurismas suelen permanecer asintomaticos hasta rotura, lo que les convierte en una enfermedad muy peligrosa, con una mortalidad media asociada de más del 80%. Recientes campañas experimentales llevadas a cabo sobre las capas que forman el tejido aórtico sugieren que, en arterias envejecidas y arterias con hiperplasia intimal, la capa interna de la aorta incrementa significativamente su espesor y rigidez, siendo capaz de soportar cargas externas. No obstante, hay muy pocos estudios computacionales sobre el aneurisma de la aorta abdominal que tengan en cuenta la contribución mecánica de las tres capas que forman el tejido arterial. En este proyecto técnico se propone un modelo de elementos finitos tricapa desde el estado tensional más simple, el uniaxial, hasta modelos que involucran geometrías idealizadas de aneurisma con diferentes valores de asimetría del saco. Se realizan comparaciones entre un modelo tricapa y un modelo monocapa, cuyos parámetros constitutivos representan el comportamiento mecánico medio equivalente de las tres capas. De la misma forma, la respuesta mecánica de estos modelos es comparada con los resultados obtenidos por otros autores para estudios computacionales de aneurismas de similares características. La contribución mecánica de cada capa es también analizada en los modelos tricapa a través de la evaluación del procentaje de absorción media. Los resultados ponen de manifiesto la necesidad de considerar la inclusión de la capa intima en modelos multicapa para obtener resultados más precisos en cuanto a tensiones máximas y desplazamientos se refiere. La parte final de esta investigación contiene una simulación interacción fluido-estructura en una geometría de aneurisma idealizada, considerando un modelo constitutivo hiperelástico anisótropo para la pared arterial. Debido al elevado coste computacional que supondría modelar un ciclo cardiaco completo en un aneurisma tricapa considerando la interacción fluido-estructura, simplemente se simula un aneurisma monocapa dentro de esta parte del proyecto. Al igual que en el apartado anterior, se hacen comparaciones entre una pared arterial elastico-lineal, hiperelastica isotropa e hiperelastica anisotropa en términos de tensiones y desplazamientos máximos.

Resumo

O aneurisma da aorta abdominal é un vulto ou inchazón localizada na parte inferior da aorta, o principal vaso sanguíneo do corpo humano que nace no ventrículo esquerdo do corazón e viaxa a través do peito e o abdome ata chegar á bifurcación ilíaca, onde se separa en dous vasos de menor tamaño que reciben o nome de arterias ilíacas. Os aneurismas adoitan permanecer asintomáticos ata a rotura, o que os converte nunha enfermidade moi perigosa, cunha mortaldade media asociada de máis do 80%. Recentes campañas experimentais levadas a cabo sobre as capas que forman o tecido aórtico suxiren que, en arterias envellecidas e arterias con hiperplasia intimal, a capa interna da aorta incrementa de maneira significativa o seu espesor e rixidez, sendo capaz de soportar cargas externas. Con todo, hai moi poucos estudos computacionais sobre o aneurisma da aorta abdominal que teñan en conta a contribución mecánica das tres capas que forman o tecido arterial. Neste proxecto técnico proponse un modelo de elementos finitos tricapa dende o estado tensorial máis simple, o uniaxial, ata modelos que involucran xeometrías idealizadas de aneurisma con diferentes valores de asimetría do saco. Realízanse comparacións entre un modelo tricapa e un modelo monocapa, cuxos parámetros constitutivos representan o comportamento mecánico medio equivalente das tres capas. Da mesma forma, a resposta mecánica destes modelos é comparada cos resultados obtidos por outros autores para estudos computacionais de aneurismas de similares características. A contribución mecánica de cada capa é tamén analizada nos modelos tricapa a través da avaliación da porcentaxe de absorción media. Os resultados poñen de manifesto a necesidade de considerar a inclusión da capa íntima en modelos multicapa para obter resultados máis precisos en canto a tensións máximas e desprazamentos se refire. A parte final desta investigación contén unha simulación interacción fluído-estrutura nunha xeometría de aneurisma idealizada, considerando un modelo constitutivo hiperelástico anisótropo para a parede arterial. Debido ao eleveado custo computacional que supoñería modelar un ciclo cardiaco completo nun aneurisma tricapa, dentro desta sección do proxecto só se simula un aneurisma monocopa. Do mesmo xeito que no apartado anterior, fanse comparacións con diferentes modelos de material.

Contents

List of Figures

List of Tables

Notation

Greek letters

Γ	Boundary.
$\Omega^{S,F}$	Computational domain (F denotes fluid, S denotes solid).
$\boldsymbol{\lambda}_j$	Expansion coefficient.
$\boldsymbol{\tau}_{\mathrm{f}}$	Fluid stress tensor.
$\boldsymbol{\tau}_{\mathrm{s}}$	Kirchhoff solid stress tensor.
$\boldsymbol{f}_{\mathrm{f}}^{B}$	Fluid body force per unit volume.
$\boldsymbol{f}_{\mathrm{s}}^{B}$	Solid body forces per unit volume.
$\boldsymbol{f}_{\mathrm{s}}^{B}$	Local acceleration of the solid.
$\boldsymbol{v}_{\mathrm{f}}$	Fluid velocity vector.
δ_{ij}	Kronecker delta.
$\hat{\boldsymbol{v}}$	Moving coordinate velocity.
λ_θ	Circumferential stretch.
λ	Axial stretch.
μ_f	Molecular viscosity of the fluid.
μ	Shear modulus of the isotropic ground matrix in the undeformed configuration.
$\psi_{\mathbf{aniso}}$	Anisotropic part of the strain energy function.
$\psi_{\mathbf{iso}}$	Isotropic part of the strain energy function.
ψ	Total strain energy function.
ρ_{f}	Fluid density.
ρ_{s}	Wall density.
$\varepsilon_{\mathrm{ij}}$	Fluid strain rate.
φ	Orientation angle of each family of collagen fibers.
ξ	Referential domain in ALE formulation.
$\bar{\boldsymbol{\tau}}$	Isochoric part of the Kirchhoff solid stress tensor.
$\boldsymbol{\tau}_{vol}$	Volumetric part of the Kirchhoff solid stress tensor.
κ	Dispersion parameter of the collagen fibers orientations.

β_H	.
α_H	Default parameter of the Hilbert-Hughes-Taylor integrator.
$\boldsymbol{\alpha}_j$	Constant vector of the Radial Basic Functions.
α_R	Mass proportional damping parameter.
β	Asymmetry parameter.
β_R	Stiffness proportional damping parameter.

Latin letters

$J^{\frac{1}{3}}$	Volumetric part of the deformation gradient.
J	Determinant of the deformation gradient.
R	Radius from centreline to posterior wall of AAA.
$\bar{I}_1$	First strain invariant of the modified right Cauchy-Green tensor.
$\bar{\mathbf{F}}$	Isochoric part of the deformation gradient.
$\boldsymbol{C}$	Damping matrix.
$\boldsymbol{F}$	Force vector.
$\boldsymbol{I}$	Identity matrix.
$\boldsymbol{K}$	Stiffness matrix.
$\boldsymbol{M}$	Mass matrix.
$\boldsymbol{q}$	Set of coordinates in the undeformed configuration.
$\mathbb{P}$	Fourth-order projection tensor that furnishes the physically correct deviatoric operator in the Eulerian description.
$\mathbf{d'}_i$	Displacement field of the Radial Basis Functions control points.
$\mathbf{x}_i$	Position of a vertex in the fluid mesh.
$\mathbf{C}$	Right Cauchy-Green tensor.
$\mathbf{F}$	Deformation gradient.
$f_{b,j}$	Radial Basis Functions.
p	Hydrostatic pressure.
r_{ij}	Magnitude of the distance between two vertices of the fluid mesh.
r	Radius from centreline to anterior wall of AAA.
$\bar{E}_i$	Green-Lagrange strain-like quantity.
$\bar{I}_{4i}$	Pseudo-invariant of the Right Cauchy-Green tensor.
$\mathbf{a}_{0i}$	Direction of the mean orientation of each family of collagen fibers (unit vector).
k_1	Stress-like parameter of the anisotropic part of the strain energy function.
k_2	Dimensionless parameter of the anisotropic part of the strain energy function.
$\bar{\mathbf{C}}$	Modified right Cauchy-Green tensor.

Acronyms

AAA Abdominal aortic aneurysm.
ALE Arbitrarian Lagrangian-Eulerian.
CFD Computational fluid dynamics.
CSS Computational solid stress.
CT Computed tomography.
EIM Elastic isotropic mono-layered.
FEM Finite element method.
FSI Fluid-Structure interaction.
G&R Growth and remodeling.
H3A Hyperelastic three-layered anistropic.
HHT Hilbert-Hughes-Taylor (integrator).
HIM Hyperelastic isotropic mono-layered.
ILT Intraluminal thrombus.
IMA Intima-media-adventitia.
MA Media-adventitia.
RBFs Radial Basis Functions.

1

Introduction

1.1 State-of-the-art

An abdominal aortic aneurysm (AAA) is a balloon-like, localized enlargement of the aorta that bulges out beyond the normal diameter of the blood vessel (figure 1.1). AAAs affect about 3% of the world population over the age of 50 [1]. Associated risk factors are mostly lifestyle-related (smoking, dyslipidemia, high blood pressure), although an heritable component can also play a role. They usually remain asymptomatic until rupture, which can lead to life-threatening internal bleeding with an in-hospital mortality of about 40% and a pre-hospitalization overall mortality of 80% [2]. Repair of an AAA may be done either by open surgery or endovascular aneurysm repair (EVAR). Open repair, as any surgical procedure, may associate a non-negligible rate of complications such as bleeding during or after surgery, myocardial infarction, respiratory impairment or graft infection. On the other hand, EVAR is a minimally invasive technique that only requires small incisions in the groin, but requires a more strict postoperative surveillance over time.

The current approach to assess the risk of rupture and to determine whether the patient should undergo surgical repair or not is a dimensional criterion based on the maximum axial diameter of the lesion (aortic size). If the maximum diameter increases more than 0.5–1 cm in one year, or whether it reaches 5.0 cm in women or 5.5 cm in men, surgical repair will be necessary [3–5]. Nonetheless, about 13% of AAAs with an aortic size of less than 5 cm rupture, whereas 54% of those over 7 cm may not rupture over long periods. Therefore, a more reliable parameter is needed for the assessment of the risk of AAA rupture. Peak wall stresses are suggested by many studies [6–8] as a more suitable parameter than the current diameter criterion. However, peak wall stresses cannot be measured in complex geometries just by applying simple analytic techniques, hence, numerical modeling must be used. In this respect, the finite element analysis provides a convenient numerical tool to calculate approximate wall stresses that facilitate the evaluation of the rupture potential of AAAs.

As shown in figure 2.16c, the aortic wall consist of three layers: adventitia, the outermost layer; tunica media, which is the medial layer, and tunica intima, which is the innermost layer. In young human arteries and arteries of laboratory animals, which are experimentally used to

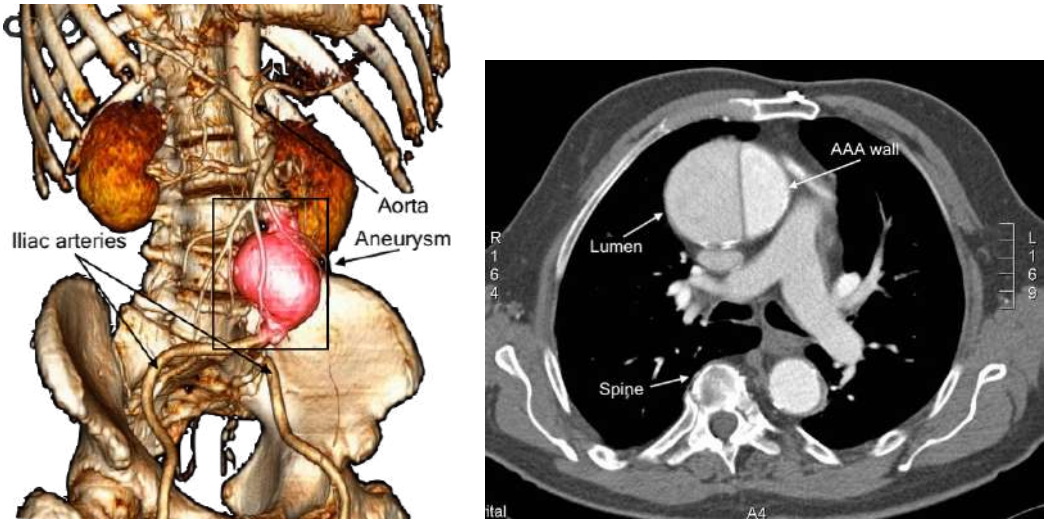

(a) Computed tomography (CT) image reconstruction of an abdominal aortic aneurysm. Front view.

(b) CT sectional cut with contrast demonstrating aneurysm dilatation and a disection of the ascending aorta.

Figure 1.1: Front and top view CT reconstructions of real AAA cases (adapted from `https://canadiem.org/`).

validate the numerical solutions, only the adventitia and media are load-bearing layers and the intima is just a thin layer made up mostly of endothelial cells. However, in aged arteries, the intima attains a significant thickness and the three layers become load-bearing. This is caused by diffuse intimal thickening or intimal hyperplasia, which is considered to be the precursor of atherosclerosis and produces the collagenization of the intima [9]. Some studies explain the thickening as a compensatory response to the wall shear reduction, so the artery decreases the luminal diameter in order to increase the blood flow and consequently restores the initial wall shear stress configuration [10]. Nevertheless, there are very few computational studies of AAAs that take into account the mechanical contribution of the intimal layer.

Even from the development of multi-layer constitutive relations for arterial walls by Holzapfel et al. [11], and the obtaining of the layer-specific material parameters by Weisbecker et al. [12], the intima has been excluded from numerical studies due to its small thickness in young arteries [13] and the high computational cost that implies the proper discretization of a highly geometric non-linear, multi-layered and thin domain. Prior studies have performed isotropic finite element simulations considering elastic or hyperelastic constitutive laws in mono-layered arterial walls, like Scotti el al. [14] and Raghavan et al. [15]. Other authors carried out more advanced computational models implementing the anisotropy of the arterial wall in patient-specific geometries like Xenos et al. [16] for a mono-layered AAA wall, Rodriguez et al. [17] for different idealized mono-layered AAAs, or Alaustre et al. [13] for a two-layered iliac artery, in which only adventitia and media were taken into account. The latest advances in medical imaging technology have made it possible

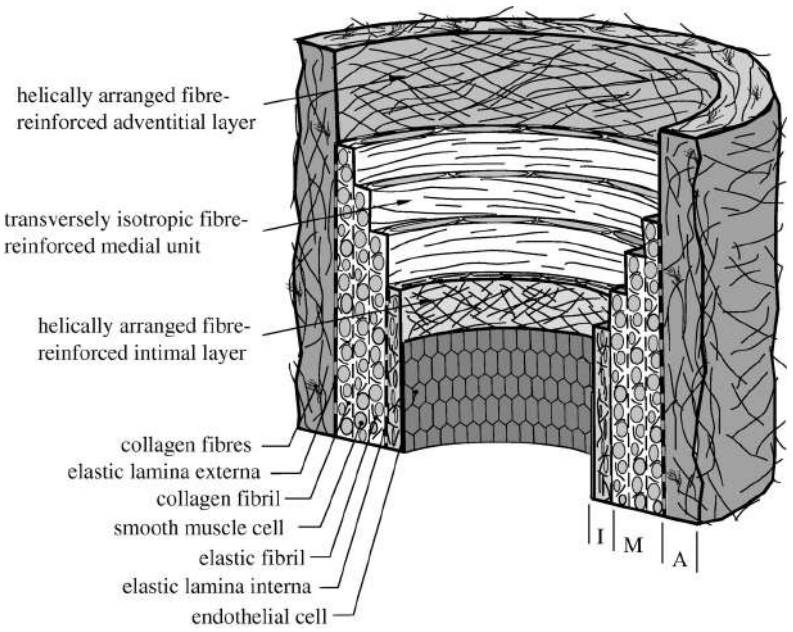

Figure 1.2: Histomechanical idealization of a healthy elastic artery with non-atherosclerotic intimal thickening (taken from [11]).

to perform not only finite element analyses on digital reconstructed patient-specific aneurysms but also experimental testing on rubber aneurysms, like Joldes et al. [18], where wall stresses were computed for different mono-layered geometries of rubber AAAs. Other studies on hyperelastic constitutive laws also include the numerical implementation of residual stresses, like Ahamed et al. [19] for evaluating wall stresses using mono-layered patient-specific geometries, or Labrosse et al. [20], where residual stresses are obtained by experimental testing on pressurized ascending, thoracic and abdominal circular samples. However, none of them consider the increase in stiffening and thickness of the innermost layer of the aorta.

The first three-layered models assumed an isotropic linear elastic response for all the layers, like Gao et al. [21, 22] for three-layered aneurysmal and non-aneurysmal aortic archs, where the Young's modulus of the medial layer was assumed to be three times larger than that of the intimal and adventitial layer. Gao et al. also peformed FSI analyses on two dimensional (2D) axisymmetric geometric models of stented three-layered aneurysms [23]. Simsek et al. [24] and Gholipour et al. [25] evaluated the rupture potential of three-layered idealized aneurysmal and non-aneurysmal geometries assuming different hyperelastic isotropic material properties for each layer. Recent studies analyzed the inclusion of residual stresses in three-layered aneurysms, like Pierce et al. [26] for a patient-specific geometry. Other researchers like Strbac et al. [27] even studied how to improve the finite element codes for computing faster, and more accurate solutions in three-layered patient-specific geometries. Nonetheless, the structural role played by tunica intima during the development of atherosclerosis has not been clarified yet.

This work proposes a three-layered model that allows to study the influence of non-atherosclerotic

intimal thickening from a mechanical point of view on different parametrized geometrical models of AAAs. The calibration of the material model, which is considered hyperelastic anisotropic, is done through finite element simulations of uniaxial tests of aorta strips cut in the circumferential and axial direction, and the inflation of plane strain aorta rings subjected to systolic blood pressure. Then, peak wall stresses and displacements are computed in three different idealized AAA geometries considering a three-layered, and an intact monolayered human aorta wall. As loading conditions, an in vivo luminal pressure waveform reproduced from [28] was applied. Additionally, comparisons between the three-layered and the intact wall are made, as well as between different material models (elastic and hyperelastic isotropic) from other studies. Finally the stiffness of each layer that make up the aneurysmal tissue is evaluated and compared through its mean stress absorption percentage.

1.2 Constitutive behavior of arterial tissue

Constitutive modeling of arterial tissue has undergone a significative evolution over the past decade. Early-modeled aneurysmal tissue was characterised as a single layer linear elastic material [29–32]. The nonlinear elastic assumption came after the uniaxial testing of aortic tissue specimens carried out by Raghavan and Vorp [33], where the mechanical behavior of the arterial wall was, for the first time, modeled as hyperelastic, with a constitutive law based on a simplified criterion derived from the Mooney-Rivlin strain energy function. Thereafter, the vast majority of the computational studies of fully developed aneurysms assumed isotropy [34–37]. A high degree of anisotropy was subsequently noticed by Vande Geest et al. [38] after performing biaxial testing to characterize the mechanical properties of aortic tissue in the longitudinal and circumferential direction. Then, the obtained experimental data would be fitted to a four parameter exponential strain function proposed by Vito and Hickey [39]. Later on, the understanding of the arterial histology by means of extensive experimental data has led to new and more accurate constitutive models that make it possible to analyze the multi-layered nature of the arterial wall as an anisotropic fiber-reinforced material [40]. The aforementioned continuum approach was considered in this study by means of the constitutive model developed by Holzapfel et al. [40] and Gasser et al. [11]. This model asserts that each artery layer may be understood as a composite reinforced material constituted by two families of collagen fibers embedded in a soft incompressible matrix, which is mostly made up of elastin. The collagen fibers are arranged in spirals and symmetrically oriented with respect to the circumferential direction. The strain energy function used to model each layer of the artery wall is given by

$$\Psi = \Psi_{\text{iso}} + \Psi_{\text{aniso}}, \tag{1.1}$$

where

$$\Psi_{\text{iso}} = \frac{\mu}{2}\left(\bar{I}_1 - 3\right) \tag{1.2}$$

$$\Psi_{\text{aniso}} = \frac{k_1}{2k_2}\sum_{i=1}^{N=2}\left[\exp\left(k_2\bar{E}_i^2\right) - 1\right] \tag{1.3}$$

with

$$\bar{E}_i = \kappa \bar{I}_1 + (1 - 3\kappa)\left(\bar{I}_{4i} - 1\right) \tag{1.4}$$

where

$$\bar{I}_{4i} = \mathbf{a}_{0i} \otimes \mathbf{a}_{0i} : \bar{\mathbf{C}}. \tag{1.5}$$

Ψ can be divided in an isotropic part, Ψ_{iso}, which represents the energy stored in the non-collagenous soft matrix, and anisotropic part, Ψ_{aniso}, which provides the energy stored in the collagen fibers. The non-collagenous soft matrix is modeled as an incompressible isotropic neo-Hookean material, with $\mu > 0$ as the shear modulus in the undeformed configuration, and $\bar{I}_1$ as the first strain invariant of a modified right Cauchy-Green tensor, $\bar{\mathbf{C}} = \bar{\mathbf{F}}^T\bar{\mathbf{F}}$, where $\bar{\mathbf{F}}$ comes from a multiplicative decomposition of the deformation gradient $\mathbf{F} = \left(J^{\frac{1}{3}}\mathbf{I}\right)\bar{\mathbf{F}}$, where $J^{\frac{1}{3}}$ and $\bar{\mathbf{F}}$ represent the volumetric and isochoric part of the deformation gradient, respectively, and $\mathbf{I}$ is a second-order unit tensor. In equation (1.3) the strain energy stored in the collagen fibers is defined as an exponential function, where N is the number of fiber families of each layer. In accordance with Schriefl et al. [41], a two-fiber family is considered for all the layers in this study. $k_1 > 0$ is a stress-like parameter, while $k_2 > 0$ is a dimensionless parameter, and both are determined from mechanical tests of the tissue. $\bar{E}_i$, which stands for the Green-Lagrange strain-like quantity, represents the strain in the direction defined by the mean orientation of each fiber family, which is in turn denoted by the vector $\mathbf{a}_{0i}$. The parameter $\kappa \in [0, 1/3]$ is also unitless and describes the level of dispersion of the fiber directions. According to the value of κ, collagen fibers may be perfectly aligned ($\kappa = 0$), which means that there is no dispersion, or randomly distributed ($\kappa = 1/3$), which corresponds with a spherical distribution of the density function and the material becomes isotropic. The three-dimensional graphical representation of the kappa density function is shown in figure 1.3. κ and $\mathbf{a}_{0i}$ are determined from histological data. Finally, $\bar{I}_{4i}$ is the pseudo-invariant of $\bar{\mathbf{C}}$.

1.3 Computational modeling

The simulations presented in this technical project were conducted by using the FEM commercial software Abaqus/Standard 6.14, in which the constitutive model explained previously is built-in [42]. To check the viability of the posed problem, different geometries were considered. From the simplest to the most complex one, we developed finite element models of uniaxial tests performed on rectangular aorta strips cut in the axial and circumferential direction, human aorta plane strain rings, and finally three different parametrized geometric aneurysms with non-atherosclerotic intimal thickening. The final part of this work contains a Fluid-Structure Interaction study of an idealized aneurysm model accomplished through implicitly coupling the aforementioned FEM code Abaqus, and the CFD solver STAR CCM+ 11.06.

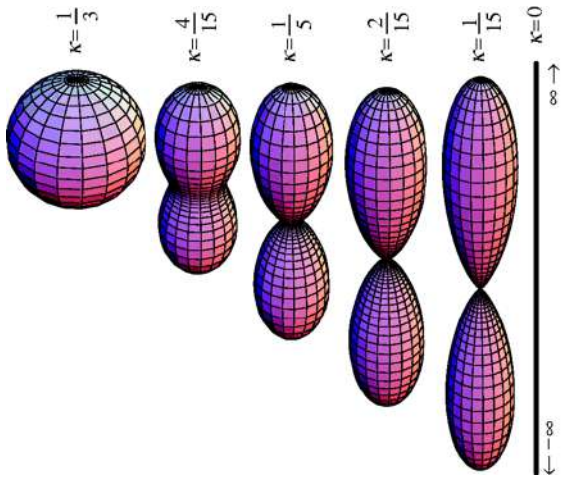

Figure 1.3: Three-dimensional graphical representation of the orientation of the collagen fibres based on the transversely isotropic density function (taken from [11]).

2

A multi-layered in-silico mode for rupture risk evaluation in abdominal aortic aneurysms

2.1 Model calibration. Finite element models of uniaxial test of aorta strips

Based on the work developed in [11], finite element computations of uniaxial tension tests were performed on rectangular intact and layer-separated aorta strips with non-atherosclerotic intimal thickening cut in the axial and circumferential direction. The specimens are loaded in the longitudinal direction and are assumed to be stress free in the undeformed configuration. The definition of axial and circumferential specimens as well as the computational model configuration are illustrated schematically in Figure 2.2, while the real test setup is shown in figure 2.1.

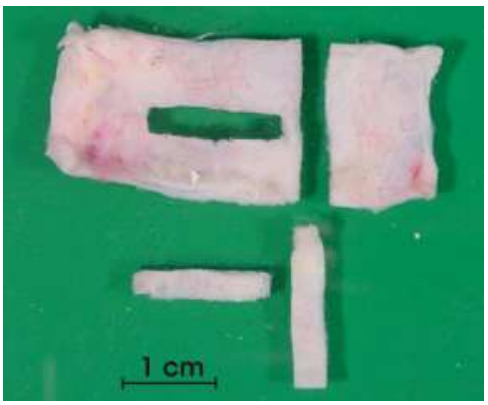

(a) Representative axial and circumferential strips excised from a disected adventitial layer of the human abdominal aorta.

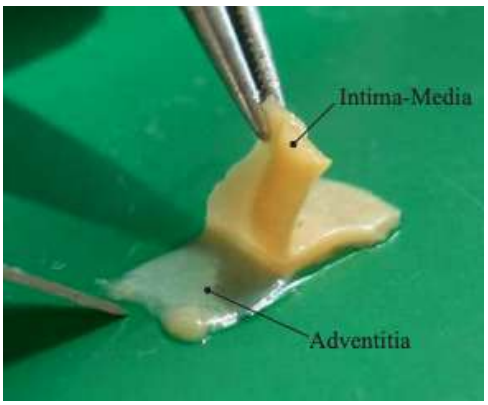

(b) Macroscopic view of an arterial wall in the axial direction, with the intima and media being separated.

Figure 2.1: Preparation of the axial and circumferential specimens during the real test (taken from [43]).

The referential dimensions of the strips were 20 mm for the length, 6 mm for the width and a different thickness depending on the layer modeled: 0.68 mm for the intima, 0.94 mm for the

media and 1.07 mm for the adventitia. The in-plane dimensions are based on the ones provided in [42], where a rectangular 10x3x0.5 mm adventitial strip is analyzed under uniaxial tension. However, since we had a maximum thickness of 1.07 mm and we wanted to keep a similar aspect ratio, the final dimensions of our strips had to be bigger in a factor of two compared to the benchmark model. Regarding the thicknesses, they are in accordance with the median thicknesses of the intima, media and adventitia determined by Weisbecker et al [12], where nine abdominal aortas from patients aged between 61 and 72 with acute non-atherosclerotic intimal thickening, were tested. The different material constants as well as the orientations of the two families of fibers considered for the layer-separated and the intact artery wall are summarized in Table 2.1.

Exploiting the symmetry of the problem, only one octave part of the geometry was modeled. To model the incompressible deformation of the arterial tissue, a total of 12,000 eight node linear solid hybrid elements (C3D8H) were used for the adventitia, 12,100 for the media and 36,000 for the intima, with a minimum of three elements through-the-thickness, whereas 220,440 elements were required for the intact layer models. Regarding the type of element used, it is important to consider the fact that, the bulk modulus of an incompressible material is much greater than its shear modulus. Due to this, a displacement-based element is not suitable since a pure hydrostatic stress state would not produce changes in the displacement field. Therefore, a mixed formulation, using not only displacement but stress variables, is required to solve the equilibrium equations. For that purpose, hybrid elements are used in our simulations to model the incompressible behavior of soft tissue, which is a realisitc assumption since it is mostly made up of water. Values of the Cauchy stresses and strains were computed for each integration point in the tensile direction. The results are compared in terms of stress vs strain curves with the experimental results obtained by Weisbecker et al. [12].

Layer	μ(MPa)	k_1(MPa)	$k_2(-)$	$\varphi(^\circ)$	$\kappa(-)$
Intima	0.044	10.14	0.00	40.5	0.25
Media	0.028	0.81	12.42	39.1	0.18
Adventitia	0.010	0.38	3.35	40.59	0.11
Intact wall	0.019	5.15	8.64	38.8	0.24

Table 2.1: Constitutive parameters for the layer-separated specimens and the intact (three-layer composite) wall of the human abdominal aorta (taken from [12]).

Figure 2.3 shows the computed Cauchy stress in the tensile direction for the circumferential (left) and axial (right) specimens at a total displacement of 2.5 mm. In agreement to the results obtained by Gasser et al. in [11] no significant change is observed in the thickness of the specimens, while the width decreases in the middle part of the strips due to the incompressibility constraint. Despite the similarity of the transition zones at the end of strips, all the specimens show a stiffer

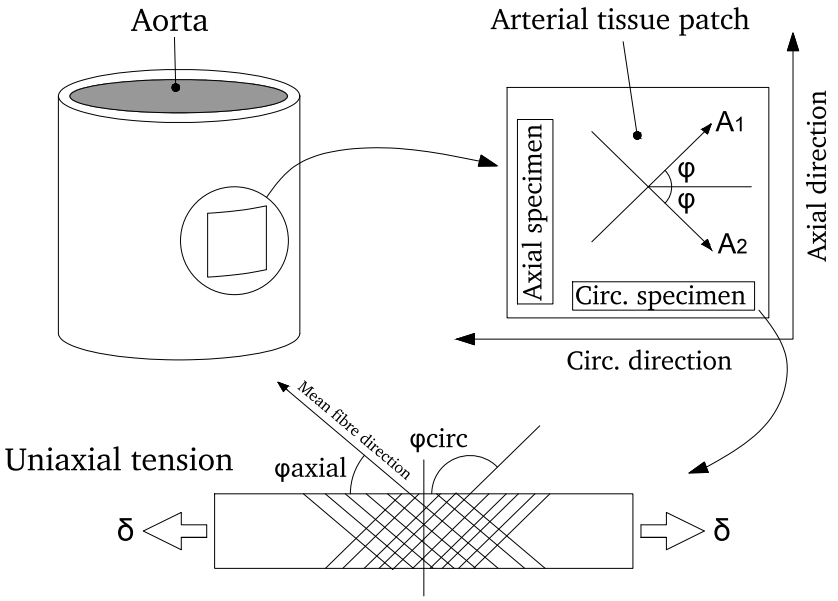

Figure 2.2: Definition of axial and circumferential specimens and uniaxial tension test configuration (adapted from [11]). A_1 and A_2 represent the mean direction of each family of fibers.

response in the circumferential direction. Tunica intima exhibits the maximum stress values of the layer-separated specimens, reaching longitudinal stresses of 6.5 MPa when it is cut in the circumferential direction. The adventitial and medial strip, with maximum values of 1 and 1.7 MPa, present a softer behavior than the intimal strip. One of the main reasons for this is the degree of dispersion of the collagen fibers, κ, which is much higher in the intima ($\kappa = 0.25$) than in any other layer. κ controls the start of the stiffening effect produced by the alignment of the collagen fibers in the direction of the applied load, therefore, higher values of κ provide a stiffer response at equal streches. Concerning the intact and the three-layered patch, we observe a parallel structural response for the first one compared to the above analysed separated intima layer: the high dispersion of the collagen fibers for this case, $\kappa = 0.24$, which is in fact very similar to the value of the intima layer, $\kappa = 0.25$, leads to a macroscopic stiffer behaviour, where fibers do not need to rotate before carrying load and just a small reduction of the width of the specimen is noticed. On the other hand, the three-layered patch shows a dissimilar mechanical behaviour in which we observe noteworthy stress discontinuities between the layers where the intima is absorbing the largest amount of stress.

Figure 2.4 shows the stress versus stretch response in the direction of the applied load for the circumferential and axial specimens. The Cauchy stress was computed as $\sigma = F\lambda/(TW)$, where F stands for the applied force, T for the thickness of the specimen, W for the width (both in the undeformed configuration), and $\lambda = l/L$ represents the stretch in the loading direction, where l and L are the lengths of the specimen in the deformed and reference configuration, respectively. The qualitative stress-stretch response is similar to the one reported by Holzapfel et al. [44]

for coronary arteries, and Weisbecker et al. [12] for the abdominal aorta. As it can be seen, the intima manifests an early exponential stiffening at low stretches in both circumferential and axial directions. This stress-stretch response is closely related to the high degree of dispersion in the collagen fiber directions previously commented, which is in turn, associated with the collagenization of the innermost hyperelastic layer during the development of the diffuse intimal thickening of the aorta [9]. Media and adventitia curves show a softer behavior in both directions, where the exponential stiffening produced by the anisotropic contribution of the collagen fibers to the strain energy function is delayed in comparison to the intimal layer. For a total Cauchy stress of 0.7 MPa, the axial specimen of the intimal layer reachs a maximum stretch of 1.24, while adventitial and medial strips have maximum streches of 1.45 and 1.5, respectively. As for the three-layered tissue, despite being made up of intima, media and adventitia, its mechanical reaction is somewhat less stiff in comparison with the intima and the intact wall, probably due to the loss of strain energy produced during the discontinuous stress migration from tunica intima to the other two layers. When comparing our computational results to the curves experimentally obtained by Weisbecker et al., we observe qualitative similarities in the general structural behavior for all the layers, except for the intact specimen. Regarding the layer-separated strips, we see a similar structural response for intima, media and adventitia, with a maximum error of 5% for the medial strip cut in the axial direction. However, the computed stress-stretch curve for the intact aorta strip cut in the circumferential direction does not match to the experimental ones at all. The calculated response in the circumferential direction for the intact strip is 78% stiffer than the real one, probably because the vast majority of the families of collagen fibers are oriented closer to the axial direction rather than the circumferential, so the assumption of a pure circumferential alignment has no physical sense. On the other hand, for the intact specimen cut in the axial direction we got a maximum error of 38%, which we consider is assumable since the dimensions of the specimens and the load are not the same.

2.2 Human aorta plane strain rings

Before assessing the effects of the intimal thickening in an AAA geometry, a simpler case is studied. To test the feasibility of the models proposed, a human aorta plane geometry was modeled with the configuration shown in figure 2.5. The dimensions of the rings were 10 mm for inner radius and a different thickness depending on the layer modeled. For the layer-separated rings the thickness of each layer is the same as the ones used previously for the uniaxial test simulations: 0.68, 0.94 and 1.07 mm for intima, media and adventitia, respectively. Plane strain boundary conditions were applied for all the models.

In order to simulate the end-systolic state, in which the artery undergoes the largest wall stresses, an internal pressure of 16 kPa (120 mmHg) was implemented. Material constants for the layer-separated and intact three-layer composite artery wall are collected in Table 2.1. Regarding the layer-separated models, 1,215 eight-node solid hybrid elements (C3D8H) were used for intima, 486 elements for the media and 748 elements for the adventitia, with a minimum of two elements

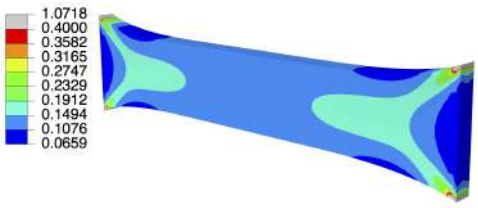

(a) Adventitial strip cut in the circ. direction.

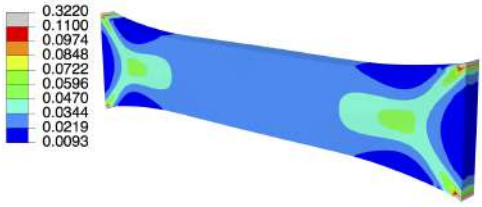

(b) Adventitial strip cut in the axial direction.

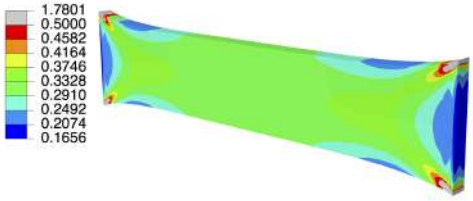

(c) Medial strip cut in the circ. direction.

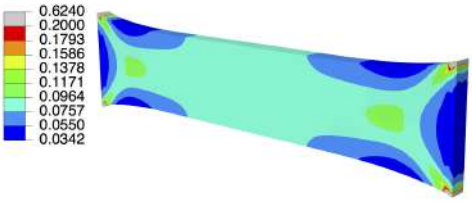

(d) Medial strip cut in the axial direction.

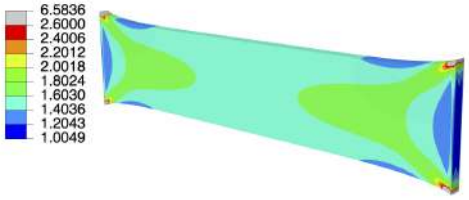

(e) Intimal strip cut in the circ. direction.

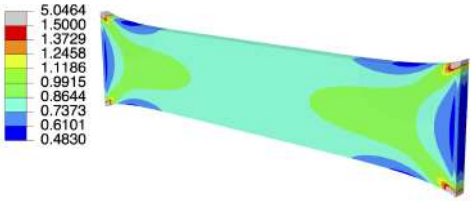

(f) Intimal strip cut in the axial direction.

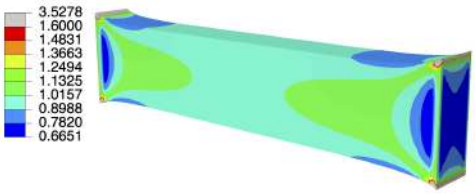

(g) Three layer composite intact patch cut in the circ. direction.

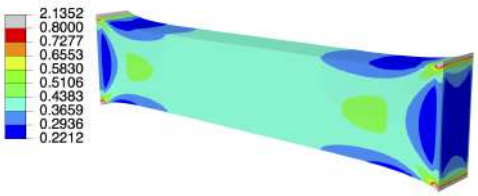

(h) Three layer composite intact patch cut in the axial direction.

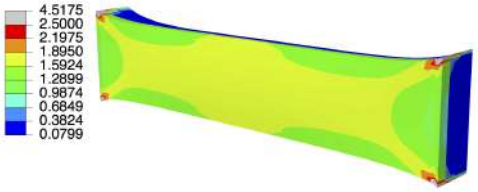

(i) Three-layered patch cut in the circ. direction (intima side).

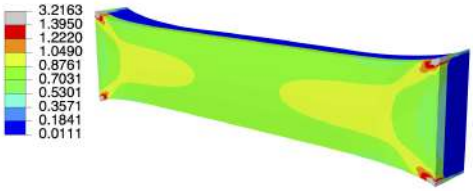

(j) Three-layered patch cut in the axial direction (intima side).

Figure 2.3: Finite element computations of the Cauchy stress in the tensile direction at a displacement of 2.5 mm. The magnitude of the depicted stress field is given in MPa. The grey zones are a result of edge effects caused by the stress concentrations due to the displacement constraint applied on the lateral face of the specimen.

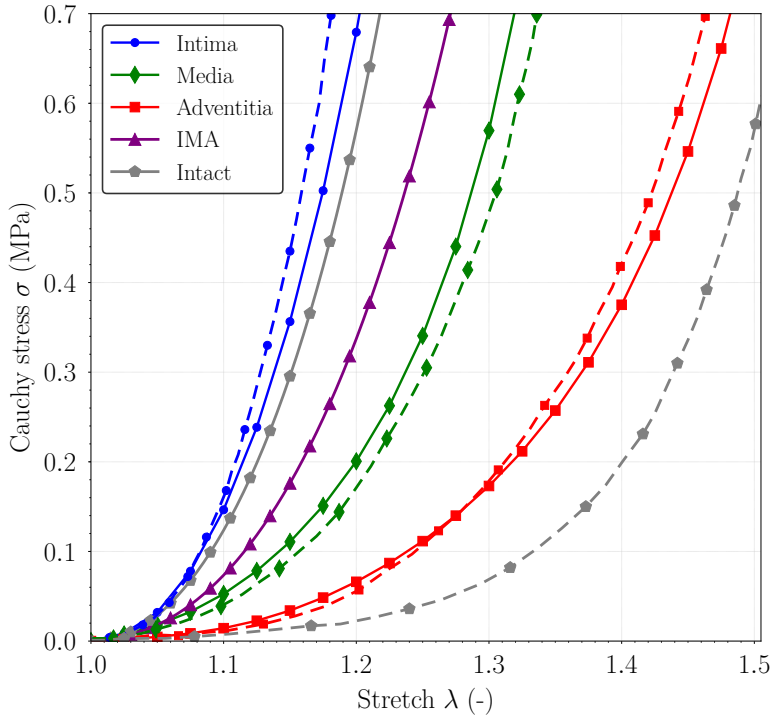

(a) Circumferential specimens.

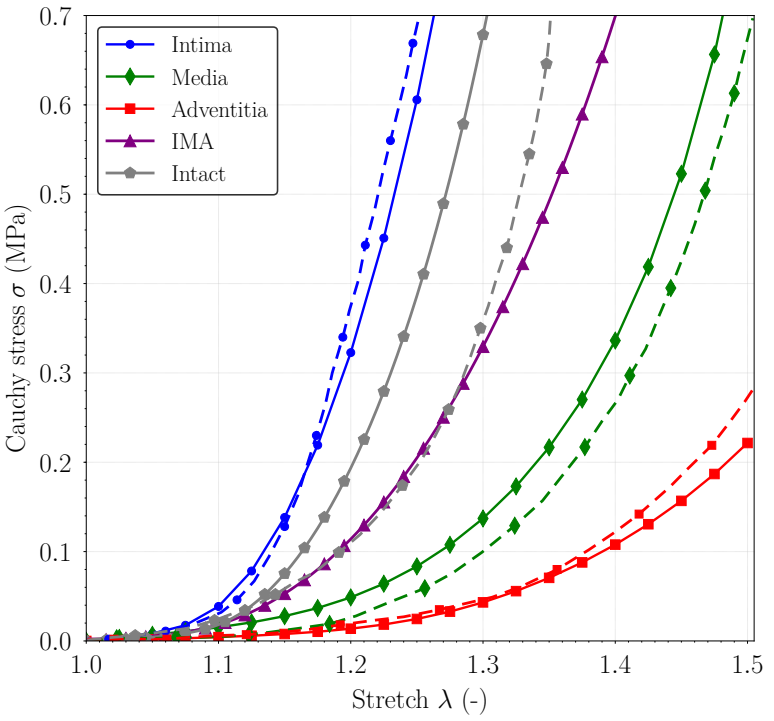

(b) Axial specimens.

Figure 2.4: Computed Cauchy stress vs stretch curves of the circumferential and axial specimens (solid curves) and comparison with the curves experimentally obtained by Weisbecker et al. [12] (dashed curves). IMA (intima-media-adventitia) represents the three-layered tissue patch

through-the-thickness of each layer. In the intact aorta rings a total of 5700 elements were required. Circumferential stresses and stretches were computed at each integration point across the thickness of the artery wall.

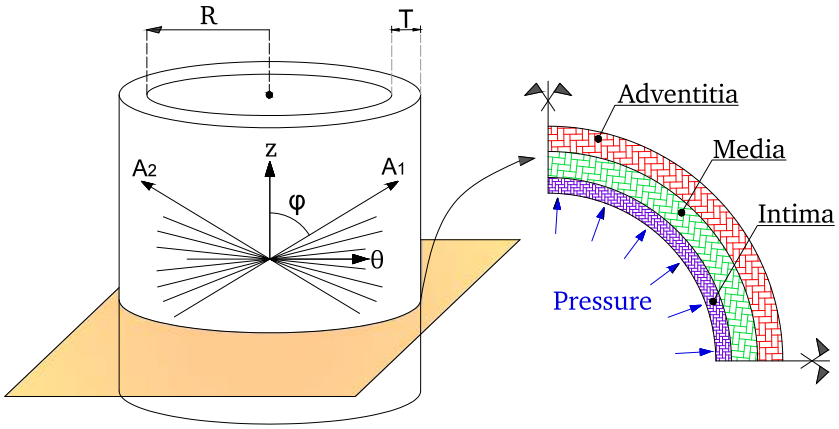

Figure 2.5: Scheme of the model configuration for the human aorta plane strain rings (adapted from [11]).

The computed circumferential stresses produced by an internal pressure of 16 kPa (120 mmHg) are depicted in Figure 2.6. The absence of residual stresses leads to a pure tension state through the whole thickness in both the layer-separated and three-layered configurations. Regarding the layer-separated rings, we observe maximal values at the inner radius of the adventitial ring of about 0.322 MPa, which decrease to 0.24 MPa at the outer, while the stress distributions of the media and intima are quite similar at the inner radius, reaching values close to 0.32 MPa, but differ from the outer radius, where the intima shows slightly higher circumferential stresses that go up to 0.28 MPa. Furthermore, we notice big differences between the through-the-thickness circumferential stresses of the intact artery, the two-layered and the three-layered rings, which are depicted in Figure 2.7. As it can be seen, the intact artery shows an analogous non-linear stress distribution to the one observed previously for the layer-separated cylinders, with a range of stress values that goes from 0.017 MPa at the inner surface to 0.012 at the outer. On the other hand, in agreement with Alastrué et al. [13], we observe again "the discontinuities caused by the heterogeneity of the two-layered and the three-layered wall". As shown in Figure 2.7, the existing stress value of 0.224 MPa at the inner part of the intima suddenly drops at the interface with the media, where it took a value of 0.04 MPa. In the same way, another stress jump is found at the interface between media and adventitia, but this time not as important as the previous one, dropping from 0.04 to 0.02 MPa.

The results in terms of internal pressure versus circumferential stretch (p_i/λ_θ) are illustrated in Figure 2.8. Once more we can see how the internal pressure/circumferential stretch response tends

to stiffen with increasing κ. As we saw in the uniaxial tests, with an early exponential stiffening, tunica intima is acting again as the stiffest layer, giving a total circumferential stretch of 1.11 at an internal pressure of 16 kPa, while the adventital layer is the softest with a final stretch of 1.34 for the same internal pressure. The medial layer shows a delayed structural response that is between the intima and the adventitia, reaching stretch values of 1.25. The three-layered and the intact rings have a similar pressure/stretch behavior, even if the former one is much stiffer despite the large stress discontinuities at the interfaces between the layers which produce a decrease of the stored strain energy in the collagen fibers.

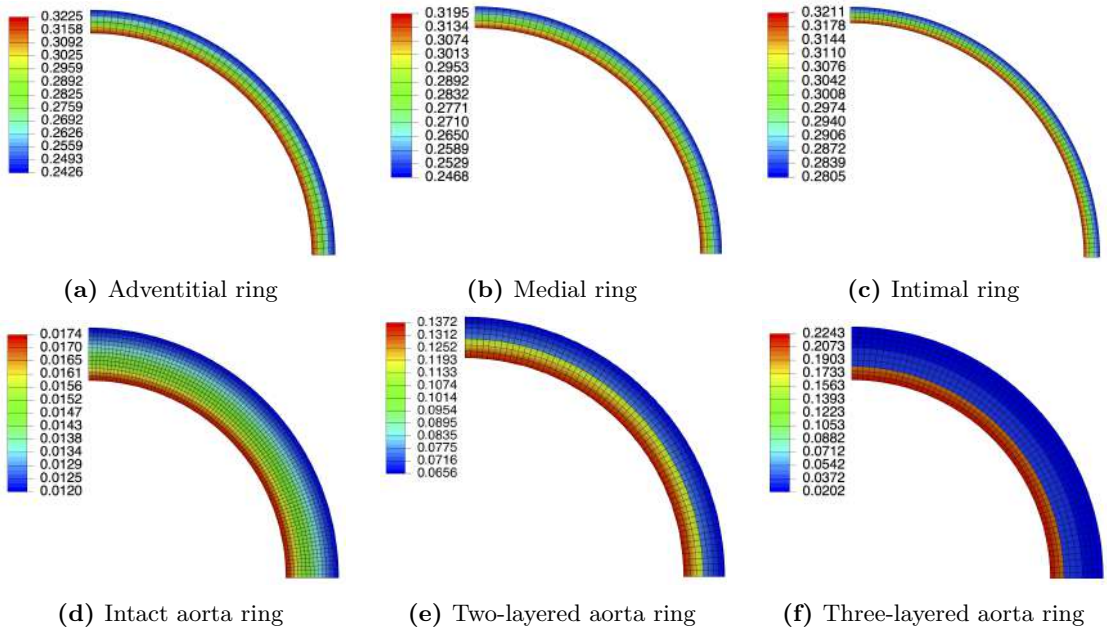

(a) Adventitial ring **(b)** Medial ring **(c)** Intimal ring

(d) Intact aorta ring **(e)** Two-layered aorta ring **(f)** Three-layered aorta ring

Figure 2.6: Circumferential stress distributions in the aorta plane strain rings at an internal pressure of 16 kPa. The magnitude of the stresses is given in MPa.

2.3 Parametrized idealized geometrical models of AAAs

Once the effects of intimal thickening have been assessed in simpler geometries, a more realistic shape is needed to take into account the influence of the typical geometrical non-linearity that characterises fusiform aneurysms, which are the most common ones. For this purpose, an in-house code [45] was developed. This code uses the application program interface of the open source CAD/CAE package SALOME [46] to create the digital model of three-dimensional extruded solid geometries. The code considers all the geometric and physical variables that characterise an idealized aneurysm, such as length, azymuthal asymmetry, wall thickness, the undilated diameter at the inlet/outlet sections and the maximum diameter at the midsection of the AAA. The circular cross sections have the ability to rotate around the three axis, and the geometries are different in terms of wall heterogeneity and asymmetry, which are depicted by cross sections perpendicular

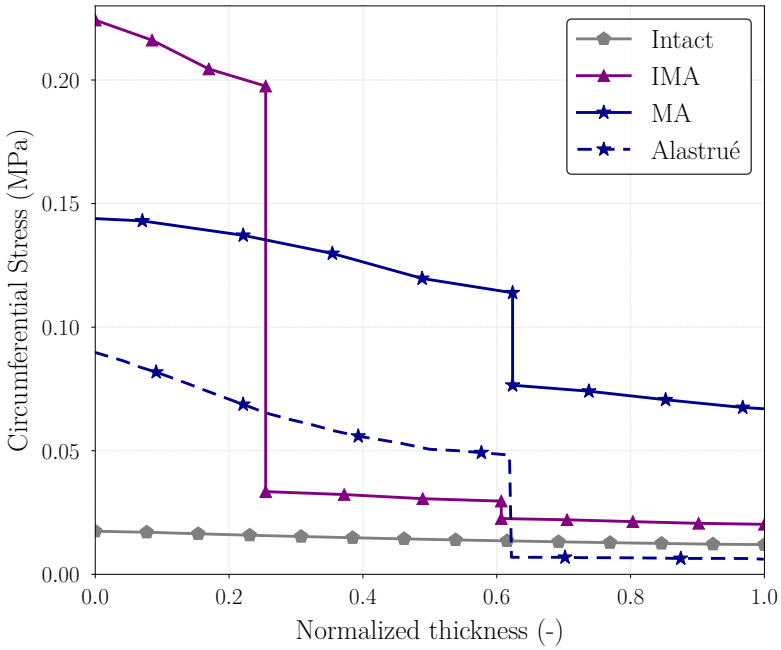

Figure 2.7: Through-the-thickness circumferential stresses of the three-layered (IMA), two-layered (MA) and intact artery rings. Comparison with the results obtained by Alastrué et al. [13] for a two-layered human iliac artery plane strain ring when an internal pressure of 13.3 kPa is applied without residual stresses.

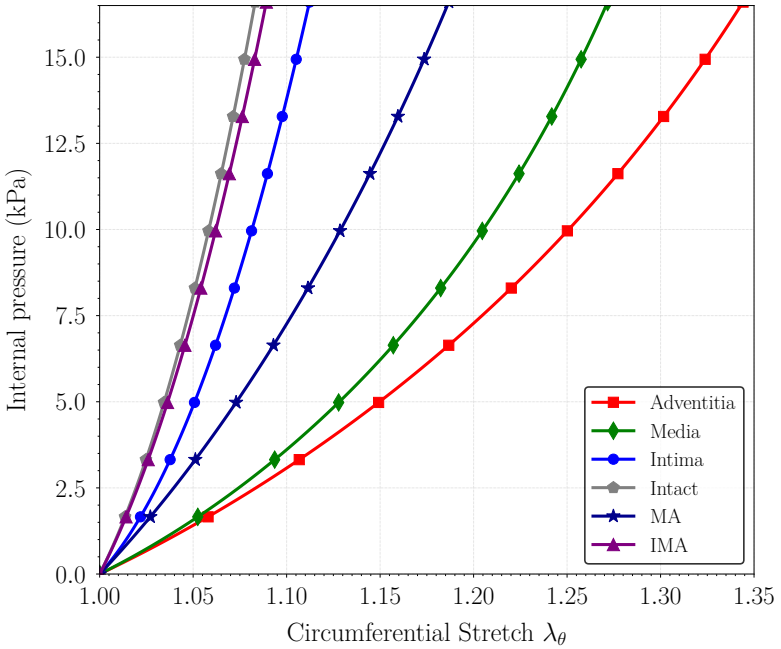

Figure 2.8: Computed internal pressure versus circumferential stretch of the aorta rings at an internal pressure of 16 kPa.

to the z-axis, hence coinciding with its centerline. The asymmetry is given by β and is defined as $\beta = r/R$ and schematically illustrated in Figure 2.9 as originally proposed by Vorp et al. [7], where r and R are the radius measured at the midsection of the AAA cavity from the longitudinal z-axis to the posterior and anterior walls, respectively. An aneurysm for which only the anterior wall is dilated whereas the posterior wall is approximately flat, corresponds to a value of $\beta = 0.2$. A value of $\beta = 1.0$ corresponds to azymuthal symmetry (figure 2.9).

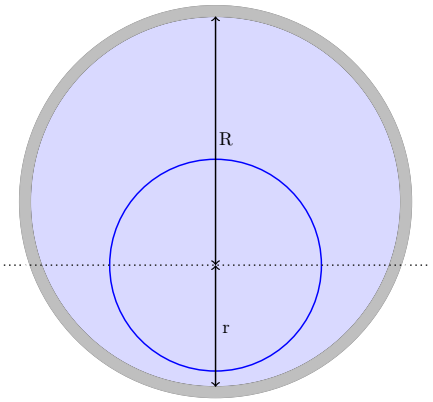

Figure 2.9: Graphical description of the azymuthal asymmetry.

Following the aforementioned procedure, three different geometries of AAA models with a total length of 23 cm were generated, varying the value of the asymmetry parameter between $\beta = 1.0$ (azymuthal symmetry) and $\beta = 0.2$ (only the anterior wall is dilated), with a medium value of $\beta = 0.6$. A value of $d = 2$ cm was adopted for the undilated diameter at the inlet and outlet sections and a maximum diameter of 6 cm was considered at the midsection of the AAA sac. The common value used from a clinical outlook to recommend surgical repair or endovascular intervention is AAA transverse diameter between 5 and 6 cm [47]. Consequently, a maximum diameter of 5.5 cm was chosen for this study, since it is comparable to the largest transverse dimension for assessment of rupture potential. Considering that this is not a patient-specific study, the uniform wall thickness assumption seems to be reasonable. In this manner, a total constant wall thickness of 2.67 mm has been adopted in all the geometries. For the layer-separated models, the thicknesses for intima, media and adventitia remain the same as the ones considered previously (0.68, 0.94 and 1.05 mm). The resultant geometries are depicted in Figure 2.10.

The effect of the luminal pressure exerted by the pulsating blood flow was simulated by a time-dependent pressure waveform. Time dependency is given by a Fourier series representations of the waveforms, and is generalized as

$$f(t) = A_0 + \sum_{k=1}^{n} \left[A_k \cos(2\pi k t) + B_k \sin(2\pi k t) \right] , \tag{2.1}$$

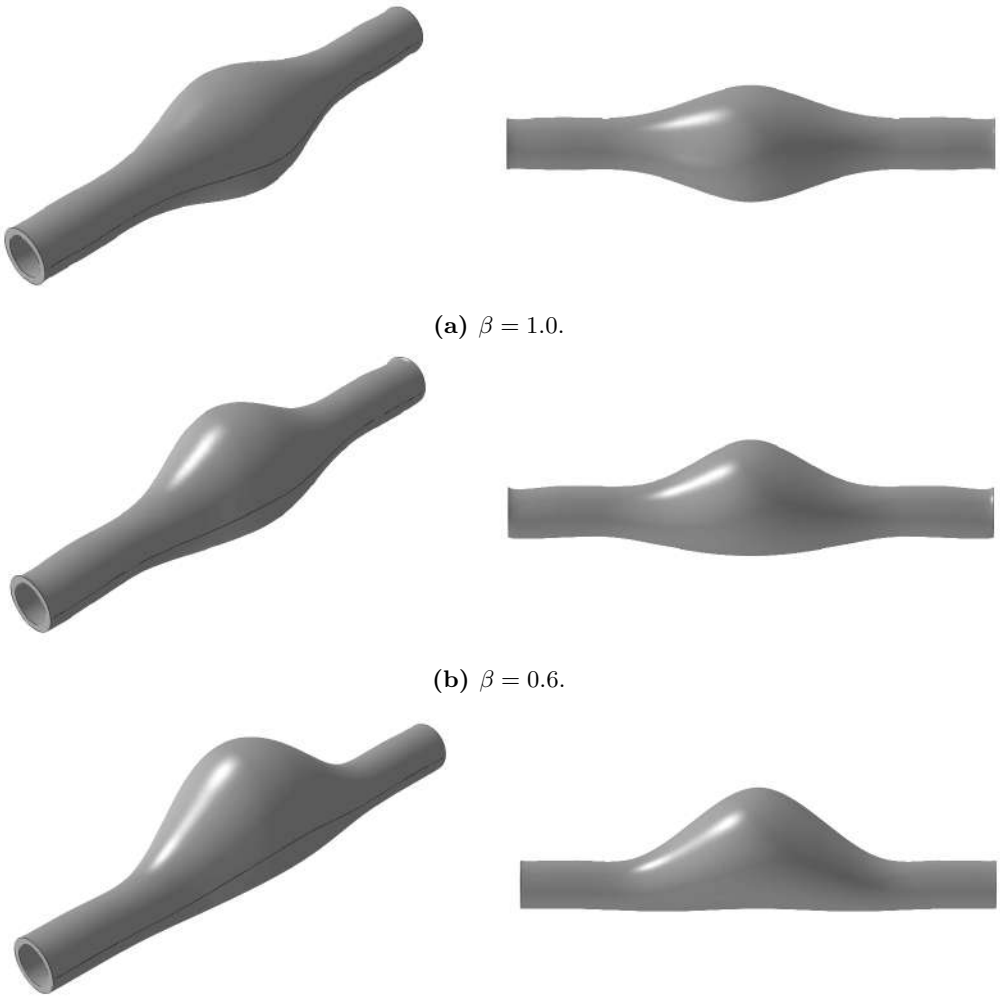

(a) $\beta = 1.0$.

(b) $\beta = 0.6$.

(c) $\beta = 0.2$.

Figure 2.10: Idealized geometries of the AAA models considered in the study.

where n is the number of harmonics used to reproduce the in vivo measurements of luminal pressure (n = 7) [14]. This waveforms are triphasic pulses first reported by Mills et al. [28], and are depicted in Figure 2.11.

Applying proper boundary conditions referred to a cylindrical coordinate system, the constraining effect caused by the iliac and renal arteries was simulated by imposing zero longitudinal displacement at both ends of the undilated sections [7]. Even though this type of boundary conditions smooths the numerical response [17], the length of the AAA must be enough not to produce stiffening effects along the geometry and stress concentrations at the proximal and distal parts. The three-dimensional AAA geometries were meshed using *ABAQUS/CAE* preprocessor

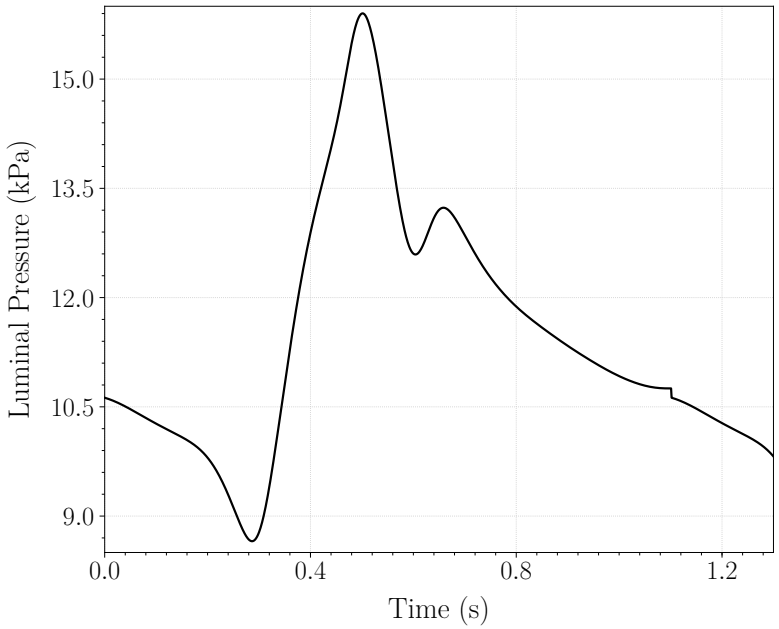

Figure 2.11: In vivo luminal pulsatile pressure waveform applied in the dynamic model. Peak systolic pressure occurs at $t = 0.5$ seconds and has a value of 16 kPa. Reproduced from [28] and [14].

with a minimum of three linear solid hexaedral hybrid elements (C3D8H) across the thickness of each layer. Table 2.2 shows a quantitative summary of the meshes with the total number of elements and nodes used for each AAA model.

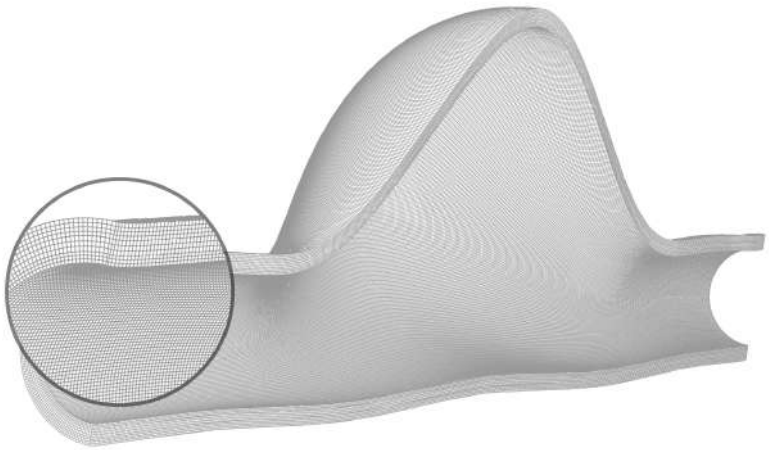

Figure 2.12: Sagittal view of the typical mesh used for the simulations. This geometry corresponds to $\beta = 0.2$.

AAA model	Number of elements		Number of nodes	
	Three-layered	Intact	Three-layered	Intact
$\beta = 1.0$	514,080	466,480	1,091,910	1,005,040
$\beta = 0.6$	481,500	440,608	1,017,288	949,560
$\beta = 0.2$	649,000	548,544	1,370,611	1,202,011

Table 2.2: Number of elements and nodes used in the three different parametrized geometrical models of AAAs studied.

Distributions of the circumferential stresses, as well as displacement fields in end-systolic conditions for three different values of β are depicted in Figure 2.13 and Figure 2.15, respectively (only one-half of the geometry cut by a sagittal plane is shown for clarity). First of all, it is important to mention that we have taken the circumferential stress as the prevailing stress, since the maximum principal stresses are almost perfectly aligned with the circumferential direction. This is in agreement with some data on aneurysms that identify normal stresses as a more reliable indicator than Von Mises criterion, which is not a suitable measure in this case because of the absence of shear stress [48, 49]. As it can be seen in Figure 2.13, both the intact and the three-layered artery present a stress gradient through-the-thickness of the aneurysmal wall, in which the inner surface absorbs the maximum circumferential stresses. As shown in Figure 2.14, this through-the-thickness stress variation is fairly flat for the intact artery, with maximum stress differences that go from 0.20 to 0.23 MPa in the $\beta = 0.2$ geometrical model. However, as previously noticed in the plane strain rings, the three-layered AAA models show a remarkable discontinuous gradient that is manifested in huge stress jumps at the interface between the layers, where the major stress drop is found at the interface between the intima and the media in all the models, with a maximum value of 0.54 MPa in the most asymmetric aneurysm ($\beta = 0.2$).

That said, and in good agreement with Rodriguez et al. [17], it is worth pointing out that the degree of asymmetry is rather considerable: for aneurysms with the same length, wall thickness and diameter of the undilated sections, the peak wall stresses increase by 32% from the symmetric ($\beta = 1.0$) to the most asymmetric geometry ($\beta = 0.2$). Thus, we can say that the geometry, and more specifically the asymmetry of the sac is a determining factor to rupture potential since the strongest stress gradients are always located at inflection points of the curvature. For $\beta = 1.0$ the maximum stress is distributed uniformly around the sac, as well as the highest displacements are, which is logical due to the azymuthal symmetry. In case of the $\beta = 0.6$ and $\beta = 0.2$ geometries, notable stress concentrations occur for both the three-layered and the intact wall at the superolateral part of the sac. By contrast, the maximum displacements are found in the inferior part, which is fairly flat. This phenomena responds to the principles of the membrane theory of shells: Because the artery wall can be considered as a structural element with a small thickness compared to the other dimensions, we can say that the stiffening at the inflection points is due to the combination between membrane and bending forces produced by the curvature, while the flatness of the inferior part only generates bending forces which leads to a softer response

with larger displacements. Table 2.3 summarises the peak wall stresses obtained for each model and establish a comparison, in terms of stresses and displacements, between the three-layered and the intact models with respect to the former one. Regarding the peak stress values, we observe an overall stress difference of about 30% that slightly increases with asymmetry, reaching a maximum $\Delta\sigma_{\max}$ of 35.9% for the $\beta = 0.2$ aneurysm. Contrastingly, variations in displacements decrease with the asymmetry from a noteworthy $\Delta U_{\max}$ about 54% for $\beta = 1.0$ to a insignificant difference of 0.75 % for the $\beta = 0.2$ geometry.

To assess the effects of the heterogeneity of the aneurysmatic wall and the material anisotropy, we have compared our results for the hyperelastic three-layered anisotropic (H3A) AAA wall with the results obtained by Scotti et al. [14, 50], where also peak wall stresses and displacements are analysed in parametrized aneurysms. We have chosen this study to establish a comparison, given that the parameterization of the AAA geometries is the same, considering $\beta = r/R$ to define the asymmetry of sac, and a similar systolic pressure of 15.7 kPa (118 mmHg). Comparisons are made between our H3A wall, in which each layer work independently, a elastic isotropic mono-layered (EIM) and a hyperelastic isotropic mono-layered wall (HIM), based on the Mooney-Rivlin constitutive model. The results of the comparison are collected in Table 2.4. In terms of stresses, first of all we observe how the percentage difference increases with the asymmetry: for the elastic wall (EIM) the range of difference is between 43 and 54%, while for the HIM, given that the hyperelastic wall can undergo larger deformations than the elastic one, and therefore develops higher stresses, the differences are between 38 and 51%, both maximum differences associated with the most asymmetric AAA ($\beta = 0.2$). Regarding the displacements, for the EIM wall the differences become greater as the asymmetry increases, reaching a maximum variation of 48%. Strikingly, for asymmetry values of $\beta = 1.0$ and $\beta = 0.6$ the HIM wall undergo larger deformations than the H3A wall, with a maximum difference of 9.43%, probably due to the stiffening effect produced by tunica intima in the inner surface of the artery. The displacements of the most asymmetric AAA geometries, $\beta = 0.2$, are quite similar with a small variation of just 0.75%.

One of the main advantages of the layer-separated models is that we can easily isolate each layer to see the maximum stresses of each layer. The circumferential stress distributions of adventitia, media and intima during systole are depicted in Figure 2.16c for the three different AAA models. As it can be seen, the patterns of circumferential stresses remain unchanged from the anterior to the posterior wall of the AAA in all cases, with a uniform distribution around the sac for the symmetric model, and stress concentrations at the inflection points of the curvature of the sac in the asymmetric aneurysms as previously commented, which means that, despite the significant stress jumps found in Figure 2.14, there is a strong stress transmission from the inner to the outer wall of the sac that is damped by the tunica intima, which acts as a natural stiffener for the artery. Table 2.5 summarises the percentage of stress absorbed by each layer with respect to the total circumferential stress. As shown, the intima is the stiffest layer, absorbing a minimum of 0.443 MPa and maximum of 0.645 MPa during peak systolic, which leads to stress absorptions of 80.49% and 80.42% for the $\beta = 1.0$ and $\beta = 0.2$ respectively and a mean absorption of 78.33%.

The adventitia is the softest layer, with a range of values between 0.193 and 0.251 MPa, and a mean stress absorption of 7.68%, while the media is a bit stiffer with a 11.05%. These results are in accordance with the previously analysed uniaxially loaded aorta strips and the inflated plane strain rings, where the early stiffening effect of the intima due to the high dispersion of the collagen fibers was predicted.

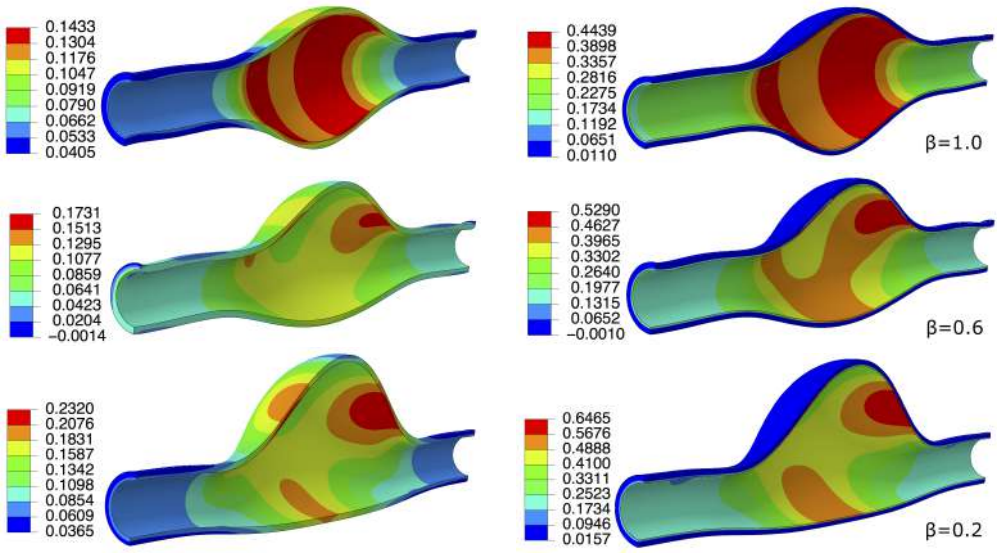

(a) Intact **(b)** Three-layered

Figure 2.13: Contour plots of the circumferential stresses in the intact and in the three-layered aneurysmatic wall for asymmetry values of $\beta = 1.0$, $\beta = 0.6$ and $\beta = 0.2$ during peak systolic. The magnitude of the stress is given in MPa.

AAA model	σ_{max} (MPa)		U_{max} (mm)		$\Delta\sigma_{max}$%	ΔU_{max}%
	Three-layered	Intact	Three-layered	Intact		
$\beta = 1.0$	0.44	0.14	2.65	1.22	31.8	53.96
$\beta = 0.6$	0.52	0.17	3.76	3.24	32.7	13.82
$\beta = 0.2$	0.64	0.23	6.65	6.60	35.9	0.75

Table 2.3: Maximum wall stresses σ_{max} and displacements U_{max} in the different asymmetric AAA models and comparison between the three-layered and the intact artery wall. $\Delta\sigma_{max}$ and ΔU_{max} show the % difference of the stress and displacement obtained with the three-layered and intact AAA models with respect to the baseline three-layered method.

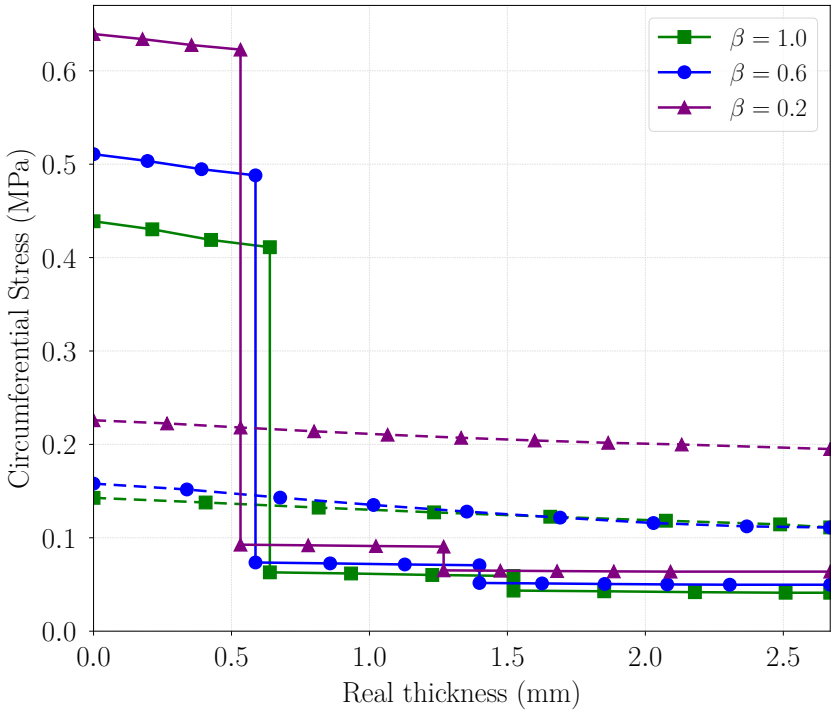

Figure 2.14: Through-the-thickness circumferential stresses in the three-layered (solid curves) and intact (dashed curves) AAA wall for asymmetry values of $\beta = 1.0$, $\beta = 0.6$ and $\beta = 0.2$.

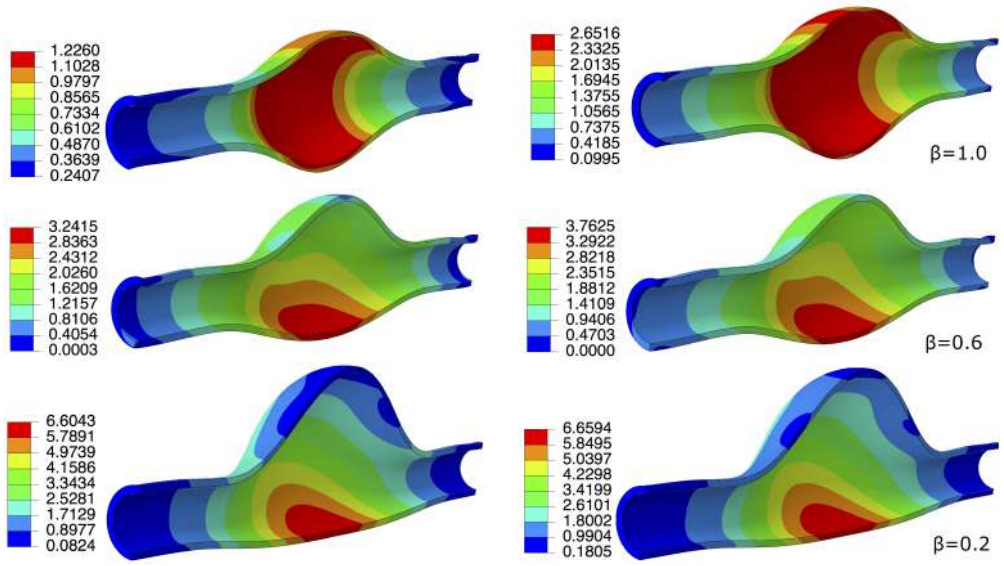

(a) Intact **(b)** Three-layered

Figure 2.15: Displacement fields in the intact and in the three-layered aneurysmal wall for asymmetry values of $\beta = 1.0$, $\beta = 0.6$ and $\beta = 0.2$ during peak systolic, in mm.

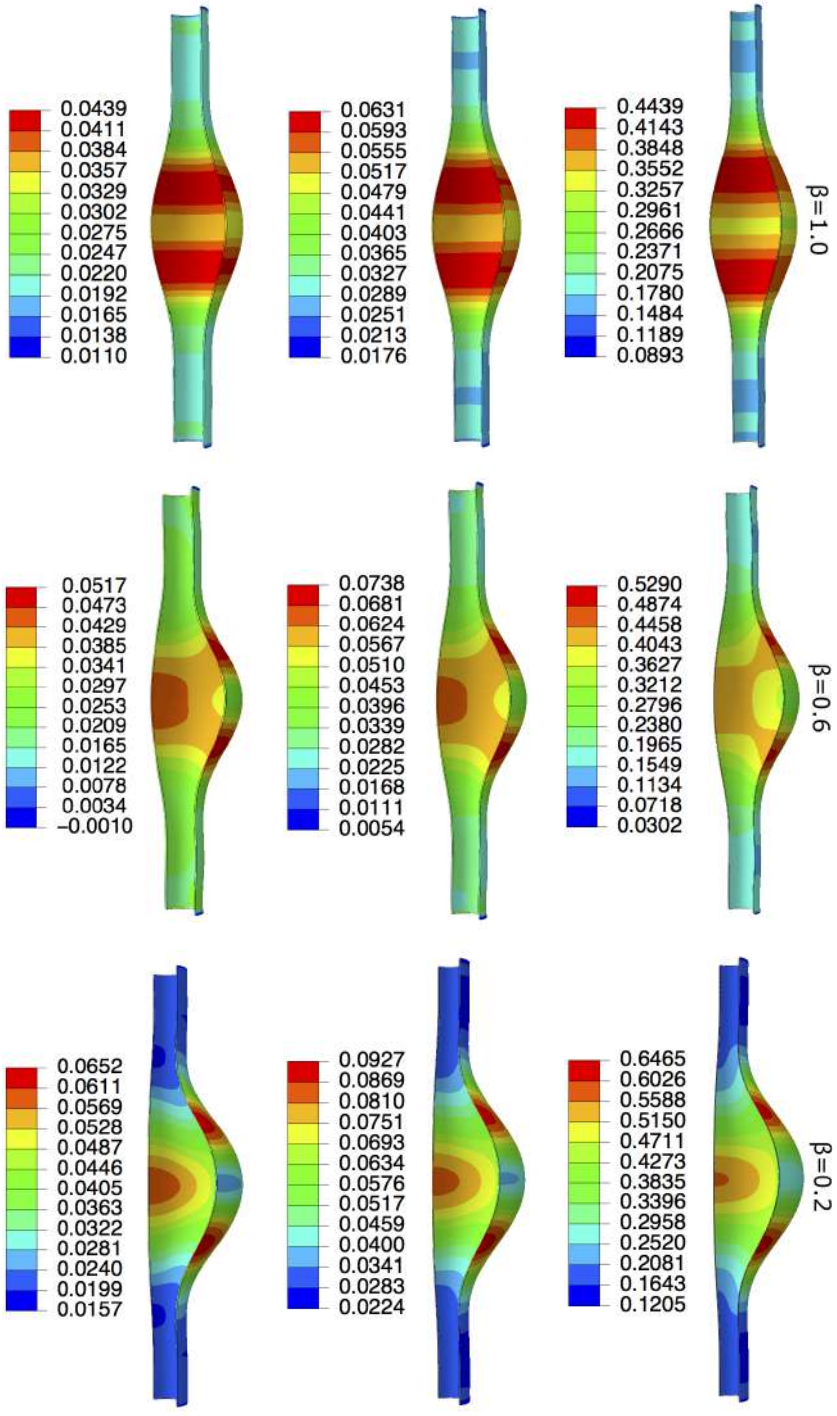

(a) Adventitia **(b)** Media **(c)** Intima

Figure 2.16: Circumferential stress distributions in adventitia, media and intima layers for $\beta = 1.0$, $\beta = 0.6$ and $\beta = 0.2$ models. The magnitude of the stress is given in MPa.

AAA model	σ_{max} (MPa)			U_{max} (mm)		
	EIM	HIM	H3A	EIM	HIM	H3A
$\beta = 1.0$	0.25(−43.18%)	0.27(−38.63%)	0.44	1.71(−35.47%)	2.90(+9.43%)	2.65
$\beta = 0.6$	0.26(−50.00%)	0.28(−46.15%)	0.52	2.50(−33.51%)	4.30(+14.36%)	3.76
$\beta = 0.2$	0.29(−54.68%)	0.31(−51.56%)	0.64	3.40(−48.87%)	6.60(−0.75%)	6.65

Table 2.4: Maximum wall stresses σ_{max} and displacements U_{max} in the different asymmetric hyperelastic anisotropic three-layered (H3A) AAA models at a peak systolic pressure of 16 kPa (120 mmHg) and comparison with the results obtained by Scotti et al. [14, 50] for the same geometries and a similar systolic blood pressure of 15.7 kPa for an elastic isotropic mono-layer (EIM) and a hyperelastic isotropic (Mooney-Rivlin) mono-layer AAA wall. The parenthesis show the % differences of the EIM and the HIM with respect to the H3A.

AAA model	σ_{max} (MPa)		
	Adventitia	Media	Intima
$\beta = 1.0$	0.043(7.83%)	0.063(11.49%)	0.443(80.69%)
$\beta = 0.6$	0.051(7.12%)	0.073(10.19%)	0.529(73.88%)
$\beta = 0.2$	0.065(8.10%)	0.092(11.47%)	0.645(80.42%)
Mean stress absorption	7.68%	11.05%	78.33%

Table 2.5: Maximum wall stresses (MPa) in adventitia, media and intima and mean percentage of peak wall stress absorbed by each layer for the three different AAA models. The parenthesis show the percentage of stress absorbed by each layer with respect to the total circumferential stress.

3

Fluid-structure interaction in abdominal aortic aneurysms

3.1 Cardiovascular fluid-structure interaction

From the structural point of view, two main loads should be considered when assessing the risk of rupture of AAAs. These are normal pressure and wall shear stress, both of them exerted by the pulsating blood flow. The effect of the former one has already been analyzed during systole in the static and dynamic finite element simulations by the implementation of the pressure waveform shown in figure 2.11, whereas, the influence of the shear stresses produced by the hemodynamic forces has not been appraised yet. Therefore, in order to obtain more reliable physiological results, a numerical approach by means of computational fluid dynamics (CFD) is required. CFD has been used successfully during the last 20 years as a versatile tool for a wide range of clinical applications, such as flow studies in compliant large vessels, medical devices like blood pumps and drug-eluting stents or examination of surgical treatments [51]. In this manner we can study the blood flow as a incompressible fluid governed by Navier-Stokes equations with Reynolds numbers at end-systolic conditions between 1 in small arterioles and 4000 in the largest artery, which means laminar flow, and moderate turbulence is shown only under weird recirculation circumstances. However, only by using CFD we cannot reproduce realistic conditions since the hyperelastic behavior of soft tissue previously explained is not taken into account. Thus, this is when Fluid Structure Interaction (FSI) comes into play.

The FSI coupling technique is among the most common computational tools in the bioengineering field for the simulation of blood flow in compliant vessels and artificial heart valves. The interaction between fluid and solid domains can be established either with a monolithic or partitioned approach (figure 3.1). In the monolithic approach, the governing equations of the fluid and solid domains are solved simultaneously at the interface using a single solver, while in the partitioned interactions, the equations are solved separately with two distinct solvers. Numerically speaking, FSI problems can be grouped by the type of coupling used into weakly (loosely) and strongly coupled algorithms, as shown in figure 3.2. In the loose or weak coupling, the fluid and solid parts are solved separately. Firstly, the received forces from the fluid domain are applied to

the structure as boundary conditions, so the structural displacements can be obtained. Then, the fluid domain is modified in accordance with the new boundaries, and the new flow field is given. The information exchange between the fluid and the structure at the interface is done only once per time step and not at every time-step. Loose coupling algorithms are usually explicit methods, since the displacement of the solid depends on the conditions of the fluid at the previous time step. On the other hand, in strongly coupled algorithms the fluid and solid parts are solved simultaneously using a monolithic scheme. To do this, the governing equations of both domains are discretized in a single system of equations, and the boundary conditions are applied on the interface. In this case, the data exchange between the solvers occurs at each iteration within a step time, which is necessary for the simulation to remain stable. This iterative communication between the fluid and and solid codes is known as implicit or "iterative staggered". Strong coupling is required when a compliant structure, like an artery, interacts with a heavy incompressible fluid, like blood [52]. In this investigation, the FSI simulations are carried out by implicitly coupling Abaqus and Simcenter STAR-CCM+. The communication is done through the SIMULIA Co-Simulation Engine (CSE). In this co-simulation, Abaqus solves the structural domain and STAR-CCM+ the fluid domain. The fluid and solid domains considered in this Chapter were also generated by means of the in-house code aneu.py [45]. The resultant geometries, as well as the definition of the different FSI boundaries, are shown in figure 3.3.

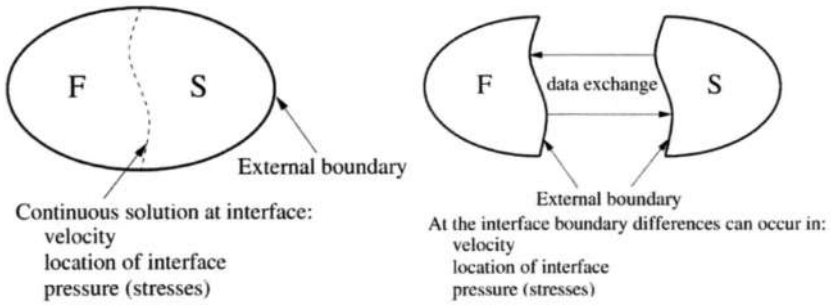

Figure 3.1: Monolithic and partitioned approach schemes (taken from [53]).

3.2 Mesh morphing. The ALE strategy

A strategy is needed for the CFD solver to account for the changes in the position and shape of the structure. The method used in this study to track the deformation of the cells that conform the fluid grid is Mesh Morphing. Morphing is done by modifying the positions of the fluid vertices in such a manner that the fluid grid can keep a reasonable quality while conforming to the solid

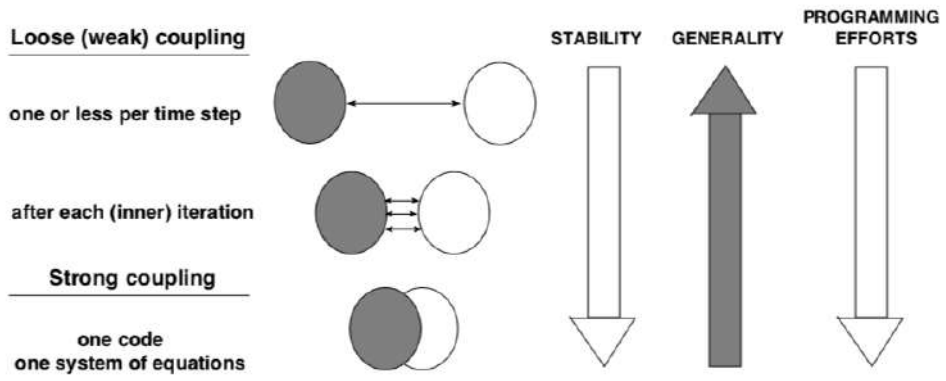

Figure 3.2: Coupling approaches for FSI (taken from [54]).

structure. This operation can be considered as topological constant, since the shape of the cells of the fluid grid can change over the time, while they maintain the same neighbours. The arbitrary motion of the mesh is taken into account by solving the fluid transport equations using the Arbitrary Lagrangian Eulerian (ALE) technique. The ALE technique combines the advantages of classical Lagrangian and Eulerian kinematical descriptions in order to lead with problems that involve large distortions of the computational domain, and get accurate solutions at the material interfaces [56]. The initialisation of the movement imposed by the morpher algorithm on the mesh is defined through a set of controls points. Each control point is related to a known displacement vector, which is used to generate a interpolation field that allows to calculate the new positions of the vertices. The interpolation method used for this purpose is called Radial Basis Functions (RBFs, in short). RBFs generates the interpolation field by a system of equations, which are created using the aforementioned control points and their displacements, where the known displacement, $\mathbf{d'}_i$, is calculated as

$$\mathbf{d'}_i = \sum_{j=1}^{N} f_{b,j}\left(r_{ij}\right) \boldsymbol{\lambda}_j + \boldsymbol{\alpha}, \tag{3.1}$$

in which $f_{b,j}\left(r_{ij}\right)$ is a radial basis function of the form

$$f_{b,j}\left(r_{ij}\right) = \sqrt{r_{ij}^2 + c_j^2} \tag{3.2}$$

and r_{ij} is the magnitude of the distance between two vertices:

$$r_{ij} = |\mathbf{x}_i - \mathbf{x}_j| \tag{3.3}$$

In the former equations, $\boldsymbol{\lambda}$ is the expansion coefficient, $\mathbf{x}_i$ is the position of vertex i, N is the number of control vertices, and c_j is the basis constant. The basis constant is set to zero in STAR-CCM+[52]. The constant vector $\boldsymbol{\alpha}$ is used to satisfy the additional constraint that

$$\sum_{j=1}^{N} \boldsymbol{\lambda}_j = 0 \tag{3.4}$$

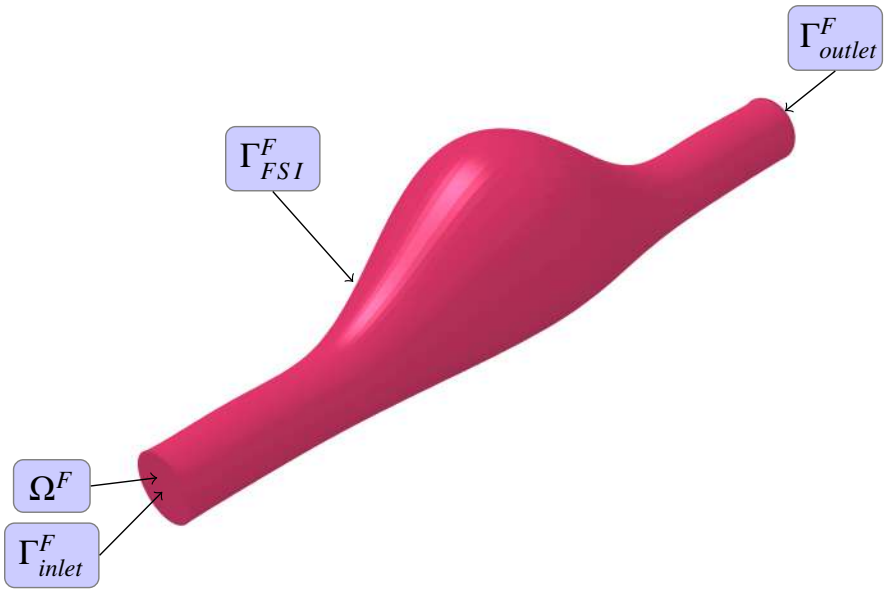

(a) Fluid domain

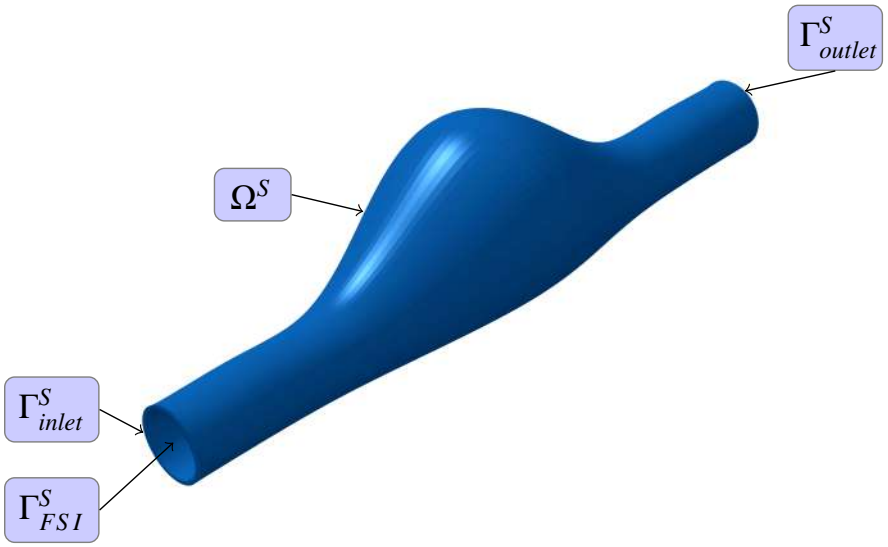

(b) Solid domain

Figure 3.3: Definition of the domains for an idealized geometric model of $\beta = 0.2$ (taken from [55]).

This additional constraint bounds the expansion for large $\mathbf{x}$. Equation (3.1) and equation (3.4) are solved to give the Cartesian components of all $\boldsymbol{\lambda}_j$ and the components of constant vector α. This results in the desired interpolation field:

$$\mathbf{d}(\mathbf{x}) = \sum_{j=1}^{N} f_{b,j}\left(r_j\right) \boldsymbol{\lambda}_j + \boldsymbol{\alpha} \tag{3.5}$$

where $f_{b,j}$ applies at all vertices in the mesh, that is

$$f_{b,j}\left(r\right) = \sqrt{r^2 + c_j^2} \tag{3.6}$$

$$r = \left|\mathbf{x} - \mathbf{x}_j\right|. \tag{3.7}$$

This equation can now be used to move mesh vertices by the calculated displacement $\mathbf{d}'$.

3.3 FSI governing equations

Since FSI is a two-field problem, its mathematical description must include the governing equations of the fluid and solid parts. In the current research, the blood flow is assumed to be an incompressible, laminar and Newtonian fluid, while for the artery wall a hyperelastic anisotropic material law will be implied on a geometrically non-linear idealized AAA model.

3.3.1 Governing equations for the fluid domain

The incompressible Newtonian fluid assumption, which is considered in this Technical Project, is mathematically described by Navier-Stokes equation. This assumption is reasonable since the blood viscosity is relatively constant at the typical high rates of shear found in the aorta [57, 58]. As commented previously, the FSI co-simulation is done by coupling Abaqus, for the resolution of the structural domain, and STAR-CCM+, for the fluid domain. The ALE methodology is automatically activated in STAR-CCM+ when a moving boundary is identified in a FSI co-simulation. The ALE formulation for momentum and mass conservation equations for the fluid domain are given by

$$\rho_{\mathrm{f}} \left.\frac{\partial \boldsymbol{v}_{\mathrm{f}}}{\partial t}\right|_{\xi} + \rho_{\mathrm{f}} \left[\left(\boldsymbol{v}_{\mathrm{f}} - \hat{\boldsymbol{v}}\right) \cdot \nabla\right] \boldsymbol{v}_{\mathrm{f}} - \nabla \cdot \boldsymbol{\tau}_{\mathrm{f}} = \boldsymbol{f}_{\mathrm{f}}^{B} \tag{3.8}$$

$$\nabla \cdot \boldsymbol{v}_{\mathrm{f}} = 0 \tag{3.9}$$

where ξ is the referential domain, and the fluid stress tensor ($\boldsymbol{\tau}_{\mathrm{f}}$) and strain rate ($\varepsilon_{\mathrm{ij}}$) are expressed as

$$\boldsymbol{\tau}_{\mathrm{f}} = -p\delta_{ij} + 2\mu_{\mathrm{f}}\varepsilon_{\mathrm{ij}} \tag{3.10}$$

$$\varepsilon_{\mathrm{ij}} = \frac{1}{2}(\nabla \boldsymbol{v}_{\mathrm{f}} + \nabla \boldsymbol{v}_{\mathrm{f}}^{T}) \tag{3.11}$$

$\boldsymbol{v}_\mathrm{f}$ is the fluid velocity vector, $\hat{\boldsymbol{v}}$ is the moving coordinate velocity, and ρ_f is the fluid density. In the ALE formulation, $\boldsymbol{v}_\mathrm{f} - \hat{\boldsymbol{v}}$ is the relative velocity of the fluid with respect to the moving coordinate velocity. The quantity p is the fluid pressure, δ_ij the Kronecker delta, and μ_f the molecular viscosity of the fluid. For the fluid domain the fluid body force per unite volume $\boldsymbol{f}_\mathrm{f}^B$ is neglected and gravitational acceleration in the streamwise direction is considered marginal.

3.3.2 Governing equations for the solid domain

In contrast to the ALE formulation for the fluid domain equations, a Lagrangian coordinate system is adopted for the solid domain. The governing equation for the solid domain is the momentum conservation given by

$$\nabla \cdot \boldsymbol{\tau}_\mathrm{s} + \boldsymbol{f}_\mathrm{s}^B = \rho_\mathrm{s} \ddot{d}_\mathrm{s}, \tag{3.12}$$

where ρ_s is the wall density, $\boldsymbol{\tau}_\mathrm{s}$ is the Kirchhoff solid stress tensor, $\boldsymbol{f}_\mathrm{s}^B$ are the body forces per unit volume, and $\ddot{d}_\mathrm{s}$ is the local acceleration of the solid. The Kirchhoff stress tensor can be decomposed as follows

$$\boldsymbol{\tau} = \boldsymbol{\tau}_{vol} + \bar{\boldsymbol{\tau}}, \tag{3.13}$$

with

$$\boldsymbol{\tau}_{vol} = Jp\boldsymbol{I} \tag{3.14}$$

and

$$\bar{\boldsymbol{\tau}} = \mathbb{P} : \tilde{\boldsymbol{\tau}} \tag{3.15}$$

where $\tilde{\boldsymbol{\tau}}$ is the fictitious isochoric Kirchhoff stress, which is written as

$$\bar{\boldsymbol{\tau}} = 2\bar{\boldsymbol{F}} \frac{\partial \Psi}{\partial \bar{\boldsymbol{C}}} \bar{\boldsymbol{F}}^T \tag{3.16}$$

where $\boldsymbol{\tau}_{vol}$ and $\bar{\boldsymbol{\tau}}$ are the volumetric and isochoric parts of the Kirchhoff stress tensor. J represents the determinant of the deformation gradient, p is the hydrostatic pressure and $\boldsymbol{I}$ the identity matrix. $\mathbb{P} = \mathbb{I} - \frac{1}{3}\boldsymbol{I} \otimes \boldsymbol{I}$ is the fourth-order projection tensor that furnishes the physically correct deviatoric operator in the Eulerian description, so that $[\mathbb{P} : (\cdot)] : \boldsymbol{I} = 0$ [11]. Ψ, $\bar{\boldsymbol{F}}$ and $\bar{\boldsymbol{C}}$ represent the total strain energy function, the distorsional part of the deformation gradient and the modified Cauchy-Green left tensor, respectively, and they have already been defined in Chapter 1.2.

3.3.3 Governing coupling equations

The FSI constraints applied to the interface (Γ_FSI) are:

1. Continuity of displacements ($\boldsymbol{u}_\mathrm{s} = \boldsymbol{u}_\mathrm{f}$).
2. Continuity of velocity ($\boldsymbol{v}_\mathrm{s} = \boldsymbol{v}_\mathrm{f}$, no slip and no-penetration condition).
3. Equilibrium of tractions ($\boldsymbol{\tau}_\mathrm{s}\boldsymbol{n} = \boldsymbol{\tau}_\mathrm{f}\boldsymbol{n}$).

3.4 Boundary conditions

The boundary conditions applied to the fluid domain are based on the ones defined by Scotti et al. in [14], and they are:

1. A time dependent fully parabolic velocity profile at Γ^F_{inlet}, where fluid enters.
2. A time dependent normal traction due to luminal pressure at Γ^F_{outlet}, where fluid leaves.
3. A slip boundary condition at the walls of the fluid domain Γ^F_{FSI}.

The pressure waveform applied to the outlet of the fluid domain is the same as the one used for the finite element simulations of parametrized idealized geometrical models of AAAs, which is shown in figure 2.11. The definition of the velocity profile applied to the inlet is done in the same way as the pressure waveform. The time dependency is also given by the Fourier series defined in equation (2.1), but this time using $N = 18$ harmonics to reproduce the in vivo measurements of luminal velocity. As shown in figure 3.4 peak systolic flow is reached at 0.4 s with a resultant flow velocity of 439 mm/s, and a pressure of 110 mmHg. The Reynolds number for the flow is 1640 based on the peak inlet velocity and 410 based on time averaged inlet velocity. All these values are in accordance with data of human abdominal aorta under resting conditions. Regarding the solid domain, the boundary conditions applied are the same as the ones explained in Chapter 2.3, where the constraining effect caused by the iliac and renal arteries was simulated by imposing zero longitudinal displacement at both ends of the undilated sections [7, 17].

3.5 Model description

This section provides a detailed description of the main numerical, and physical characteristics of the computational model. Concerning the material properties of the fluid domain, blood is modeled as a Newtonian fluid with a constant density of $\rho_{\text{f}} = 1.05$ g/cm^3 and a molecular viscosity of $\mu_{\text{f}} = 3.5$ cP, as proposed by [59]. For the arterial tissue, we assume a mono-layered hyperelastic anisotropic wall with a constitutive law given by the Holzapfel-Gasser-Ogden form [11], which has been explained in section 1.2. The material constants are summarized in and they were obtained by Weisbecker et al. [12] for an intact aortic wall, which represents the equivalent or mean mechanical behavior of a three-layer composite wall made up of intima, media and adventitia.

Layer	μ(MPa)	k_1(MPa)	$k_2(-)$	$\varphi(^\circ)$	$\kappa(-)$
Intact wall	0.019	5.15	8.64	38.8	0.24

Table 3.1: Constitutive parameters for the intact (three-layer composite) wall of the human abdominal aorta (taken from [12]).

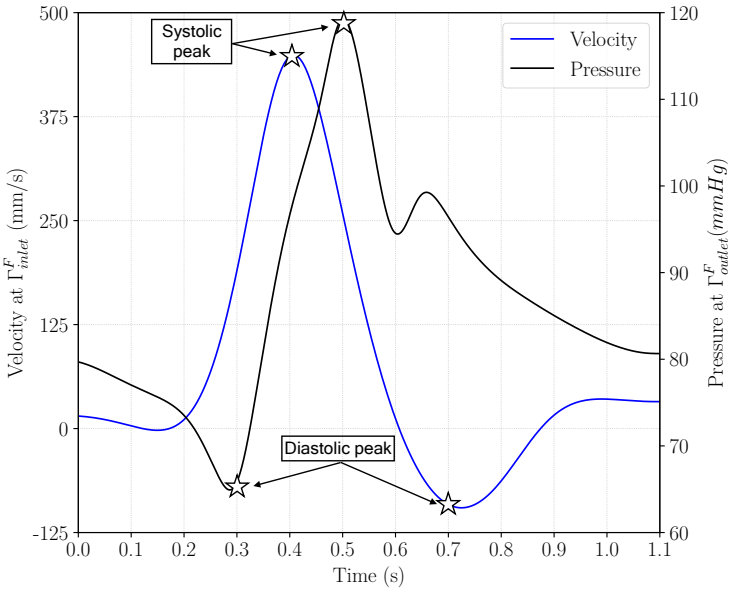

Figure 3.4: In vivo luminal pulsatile velocity and pressure waveforms applied to the inlet and outlet sections of the fluid domain. Reproduced from [28] and [14]. Data extraction points at systolic and diastolic peaks are marked with stars.

Regarding the domain discretization, a polyhedral volume mesh with a total of 117,537 cells (708,290 vertices) was used for the fluid domain, while 166,816 eight-node hybrid solid elements (C3D8H), with two elements through-the-thickness of the wall, were required for the solid part. The resultant meshes for both fluid and solid domains are depicted in figure 3.5. Computations were performed in a high performance computing (HPC) cluster with a theoretical peak performance of 7.1 TFLOPs. All fluid-structure interaction simulations where run using the asymmetric configuration 28p-12p, where the first term (28p) indicates the computing cores assigned to the solid part, while the second one (12) matches with the cores in the fluid domain. This is the fastest option (approximately 57 hours), with 2 gigabytes of physical memory assigned to each processor.

According to Fernández et al. [55], some stability problems were found during the FSI simulations. These numerical instabilities were associated to high frequency oscillations caused by the pulsatile nature of blood flow acting on a thin and soft tissue wall, and the absence of surrounding biological matter, like the spine or the stomach, that would damp the structure in a physiological environment. In order to solve this problem, the time integration scheme of the fluid and solid domains had to be changed. First of all, the discretization of the flow equations is done by means of the backward Euler strategy, since it is an unconditionally stable numerical method. On the other hand, for the time integration of the structural part, the Hilbert-Hughes-Taylor (HHT) method was used. This is a one step implicit method belonging to the integration formulas of the Newmark family, that allows for energy dissipation without degrading the order of accuracy (which is not possible with the regular Newmark method), and it is unconditionally stable [60].

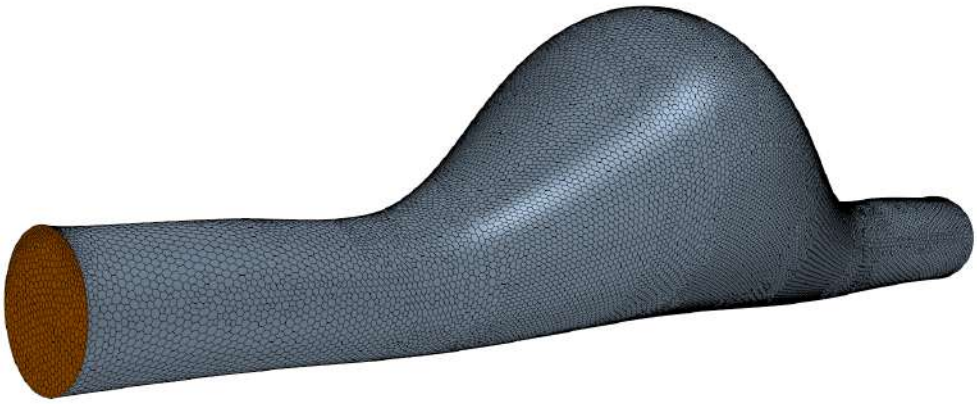

(a) Mesh for the fluid domain.

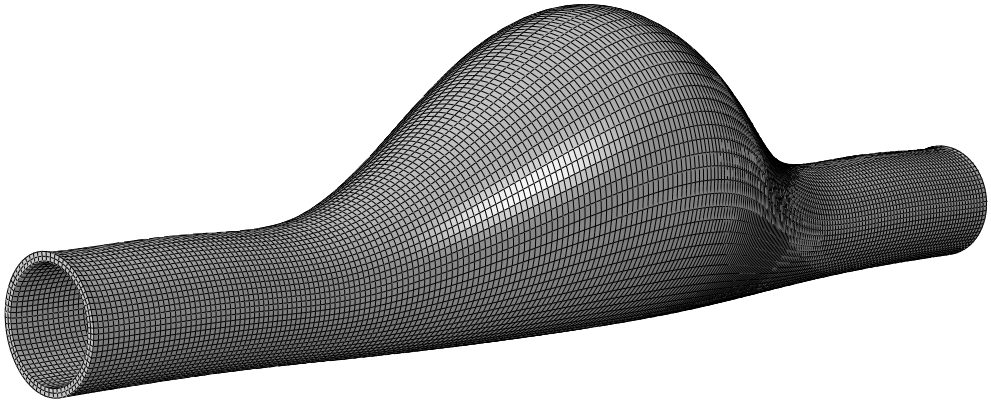

(b) Mesh for the solid domain.

Figure 3.5: Meshes for $\beta = 0.2$ idealized geometries.

The HHT integrator does not pertain the mathematical expressions of the Newmark method formulas, but the time-discrete momentum equation is modified as follows

$$\boldsymbol{M}\ddot{\boldsymbol{q}}_{n+1} + (1+\alpha_H)\boldsymbol{C}\dot{\boldsymbol{q}}_{n+1} - \alpha_H\boldsymbol{C}\dot{\boldsymbol{q}}_n + (1+\alpha_H)\boldsymbol{K}\boldsymbol{q}_{n+1} - \alpha_H\boldsymbol{K}\boldsymbol{q}_n = \boldsymbol{F}(\tilde{t}_{n+1}) \tag{3.17}$$

with

$$\tilde{t}_{n+1} = t_n + (1+\alpha_H)h \tag{3.18}$$

where $\boldsymbol{M}, \boldsymbol{C}$ and $\boldsymbol{K}$ are the mass, damping and stiffness matrices, respectively. The force $\boldsymbol{F}$ is dependent of the time, t, and $\boldsymbol{q}$ represents the set of coordinates used in the undeformed configuration. The parameters γ and β_H are calculated as

$$\gamma = \frac{1-2\alpha_H}{2} \qquad \beta_H = \frac{(1-\alpha_H)^2}{4} \tag{3.19}$$

The default values to ensure the unconditional stability and the second order accuracy of the method are summarized in table 3.2. The smaller value of α_H, the more damping is introduced in the structure. Note that if $\alpha_H = 1$ we obtain the Newmark method, and if $\alpha_H = 0$ we have the trapezoidal formula with no numerical damping.

α_H	β_H	γ
-0.3	0.4225	0.8

Table 3.2: Default parameters for the Hilber-Hughes-Taylor integrator.

Since an unstable behavior was still noticed when decreasing the time step, not only a numerical damping was induced in the structure, but a material one as well. Classical Rayleigh damping was added to the structural model to simulate the physical damping essence of the surrounding tissue. This model expresses damping as a linear combination of the mass and stiffness matrices, that is,

$$\boldsymbol{C} = \alpha_R \boldsymbol{M} + \beta_R \boldsymbol{K} \tag{3.20}$$

where α_R and β_R are the mass proportional parameter and the stiffness proportional parameter, respectively. These coefficients were selected for the first natural frequency of the aneurysm and a damping ratio of 20%, obtaining a value of 4 for the mass proportional parameter, α_R, and a value of 0.0015 for the stiffness proportional coefficient, β_R. The influence of including both, HHT integrator and Rayleigh damping, is shown in figure 3.6 and figure 3.7. The general structural damping observed in figure 3.6 is similar to the one reported Fernández et al. [55], even though our mass proportional and stiffness proportional parameters are higher since we are modeling the arterial wall as hyperelastic anisotropic, so it can undergo larger deformations and the material damping has to be greater to reproduce the physiological conditions.

3.6 Results

The results of the FSI simulations are shown in figures 3.9-3.16 in terms of circumferential stresses, displacements, flow velocities and fluid pressure distributions, for the data extraction points marked in figure 3.4 at systolic and diastolic peaks. Regarding the flow dynamics, it is clear that the blood flow is governed by the non-linear shape of the aneurysm sac, and the compliance of the vessel. From t=0 to t=0.4 s, the velocity streamlines show a pure laminar flow with absence of vortices, which is a flow path commonly associated with systolic acceleration [14]. This is due to the compliance of the vessel, which ejects the vortex downstream when the AAA cavity is fully expanded. Once systolic peak has been reached, the expansion of the sac produced by the storage of strain energy in the hyperelastic artery wall starts to decrease, causing a reverse pressure gradient that yields to flow reversal and vorticity. An example of flow reversal is shown in figure 3.8. As it can be seen, vortices start to develop in the midsection of the sac, and they travel upstream along the anterior wall towards the end of the aneurysm, where they are fully dissipated.

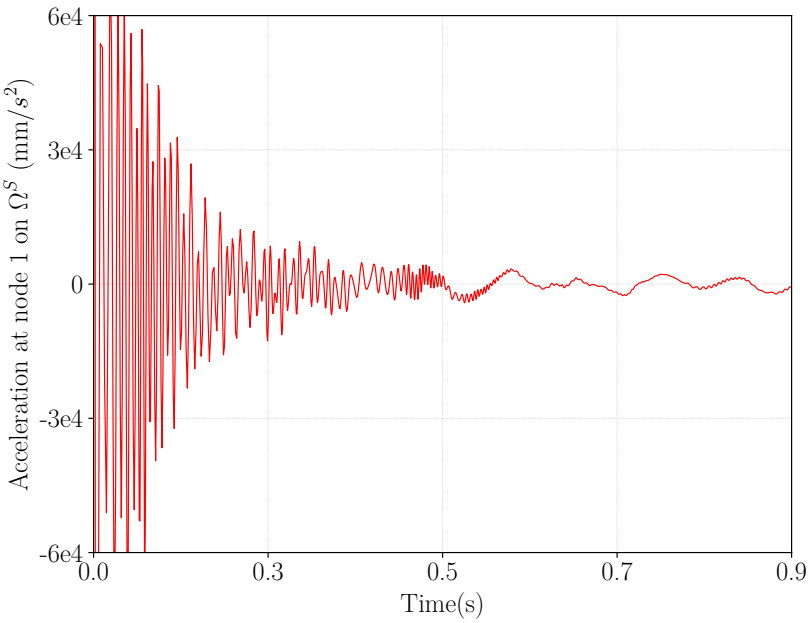

Figure 3.6: Evolution of the acceleration at node 1 (figure 3.7c), when combining the HHT integrator and Rayleigh damping.

The wall pressure distributions in the fluid are very similar to the ones reported by [50]. During systolic acceleration, the pressure gradient is given by a higher pressure at the outlet rather than at the inlet. The deceleration of the velocity inlet leads to a phase shift in the flow dynamics that produces a opposing pressure waveform. This pressure drop yields to the recirculation effects previously commented.

Concerning the stresses in the artery wall, we have chosen this time Von Mises criterion as the prevailing stress quantity to analyze the risk of rupture, since we want to account for the shear forces produced by blood flow. The stress patterns observed are very similar to the ones reported previously in figure 2.13, where the maximum values are found at the supero-lateral part of the sac, where the curvature changes. The maximum values for the Von Mises equivalent stress occur at t=0.5 s, with 0.32 MPa, while the minimum is shown during peak diastolic pressure at t=0.3 s, with 0.18 MPa. Figure 3.17 shows a comparison of the Von Mises stress evolution during a full cardiac cycle with the FSI and CSS (Computational Solid Stress) simulations performed by Fernández et al. [55], which used the same geometry and boundary conditions but different material models. First of all, we can see how the peak wall stress for the FSI-hyperelastic anisotropic, CSS-elastic and CSS-hyperelastic isotropic is delayed with respect to the FSI-hyperelastic isotropic and FSI-elastic models. The former one occurs at t=0.5, just when the peak systolic pressure is reached, while the latest appears a bit earlier at t=0.4 s. Strikingly, the hyperelastic isotropic wall reaches a slightly higher peak wall stress than the hyperelastic anisotropic wall (0.33 vs 0.32). However, the stress profile of the FSI-hiperelastic isotropic wall shows an unstable behavior with noteworthy fluctuations that would probably be damped during a longer cardiac cycle.

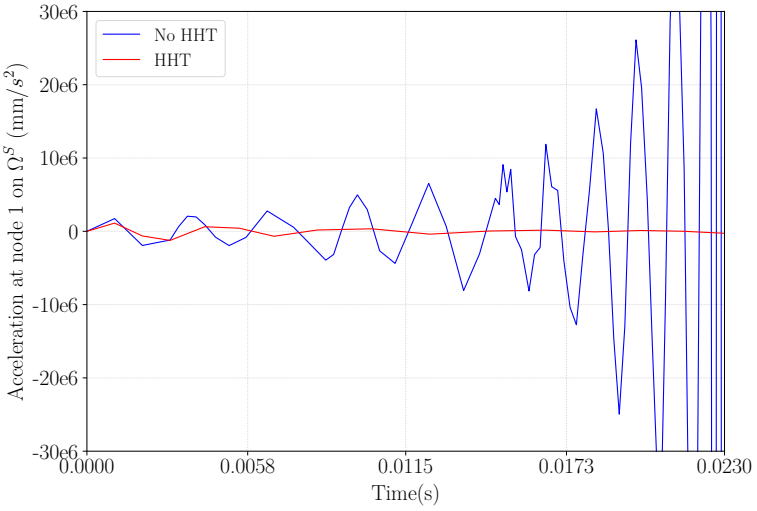

(a) Influence of the HHT integration scheme.

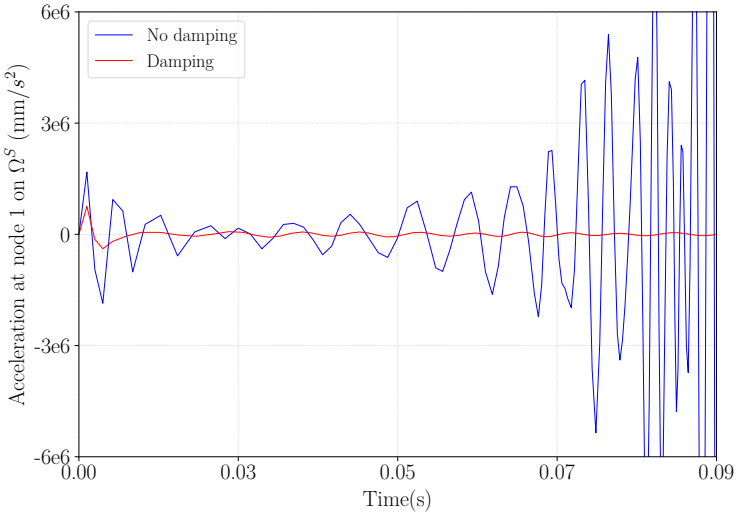

(b) Influence of Rayleigh material damping.

(c) Location of node 1 in the solid domain.

Figure 3.7: Acceleration at node 1 with and without material and numerical damping properties.

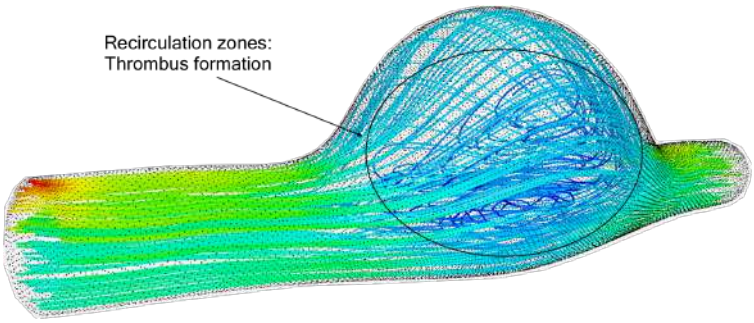

Figure 3.8: Observed recirculation zones during systolic deceleration at t=0.581 s. The reduction of shear stresses produced by flow reversal is one of the main causes of thrombus formation.

With regard to the displacements, the inclusion of blood flow shear forces acting on an isotropic tissue wall leads to a non-symmetric deformation with a significant clockwise rotation of the aneurysm sac, which is almost laid down on the XY plane. Due to this, the FSI displacement field is dissimilar to the one obtained previously for the CSS models, in which the maximum value was located at the inferior part of the sac, while this time is found in the lateral part. When comparing with other constitutive models (see figure 3.18), we observe huge differences between the elastic and hyperelastic isotropic with respect to the hyperelastic anistropic wall. Maximum displacements close to 9 mm are found in the FSI-hyperelastic anistropic models, whereas the others do not go over 3.5 mm. In order to evaluate the degree of anisotropy of the material, radial and circumferential displacements have been obtained at three different nodes in the solid domain mesh. Figure 3.19 plots the time evolution of these displacement components for the comparative node, N1, the node with maximum resultant displacement, N2, and another one located at the superolateral part of the AAA sac, N3. As it can be seen, the radial component at N3 and N2 is three times higher than any circumferential displacement. This fact indicates that, the elements near the sac sustain using in-plane membrane forces, whereas the elements close to the flat part of the geometry resist by bending stresses.

All the results in terms of stresses and displacements are summarized in table 3.3.

Technique	Max. VM stress (MPa)	Max. Disp. magnitude (mm)	Time (s)
FSI-Hyperelastic anistropic	0.32	8.47	0.5
FSI-Hyperelastic isotropic	0.33(+3.03%)	3.21(−62.10%)	0.42
CSS-Hyperelastic isotropic	0.28 (−12.5%)	2.40 (−71.66%)	0.49
FSI-Elastic isotropic	0.29 (−9.37%)	2.90 (−65.76%)	0.46
CSS-Elastic isotropic	0.25 (−24.24%)	2.35 (−72.25%)	0.49

Table 3.3: Maximum Von Mises wall stresses and resultant displacements predicted by FSI and CSS techniques for $\beta = 0.2$. The parentesis indicate the difference with respect to the FSI-hyperelastic anisotropic model.

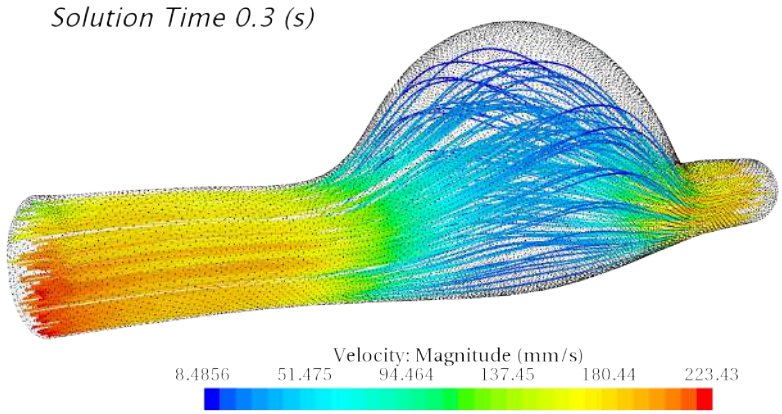

(a) Side view of velocity streamlines at t=0.3 s.

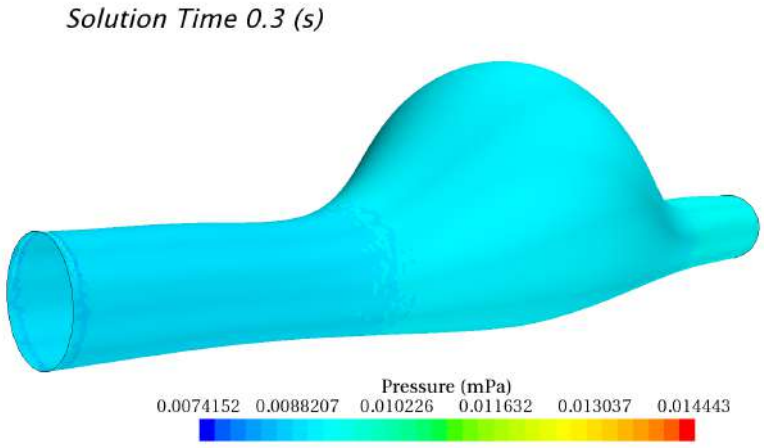

(b) Fluid pressure at the wall at t=0.3 s.

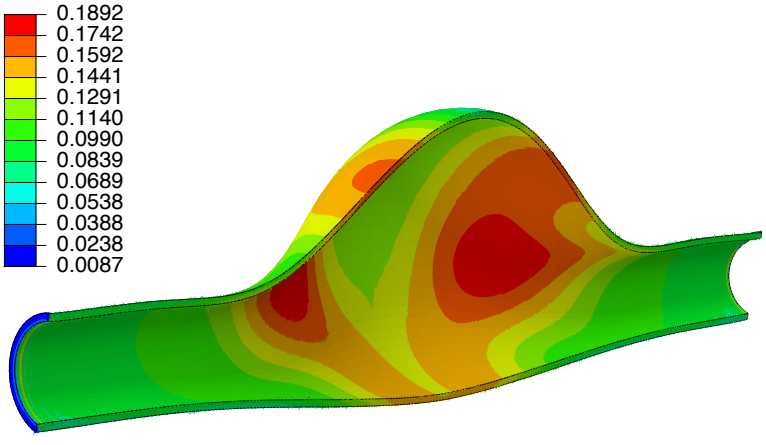

(c) Sagittal view of the Von Mises stress distribution at t=0.3 s, in MPa.

Figure 3.9: Wall stress results for $\beta = 0.2$ at pressure diastolic peak.

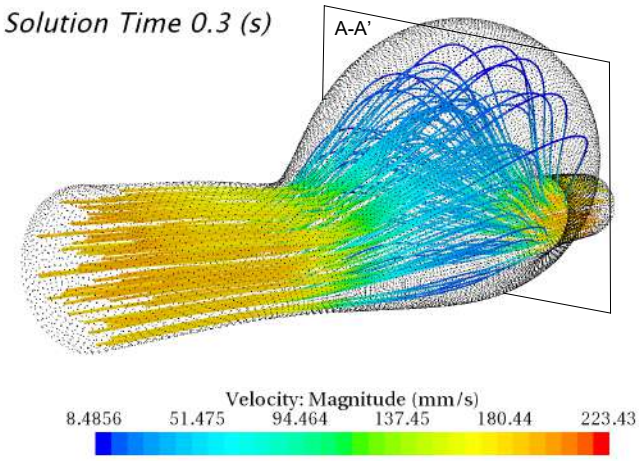

(a) Perspective view of the velocity streamlines at t=0.3 s. The sectional cut A-A' is depicted in the undeformed configuration of the sac.

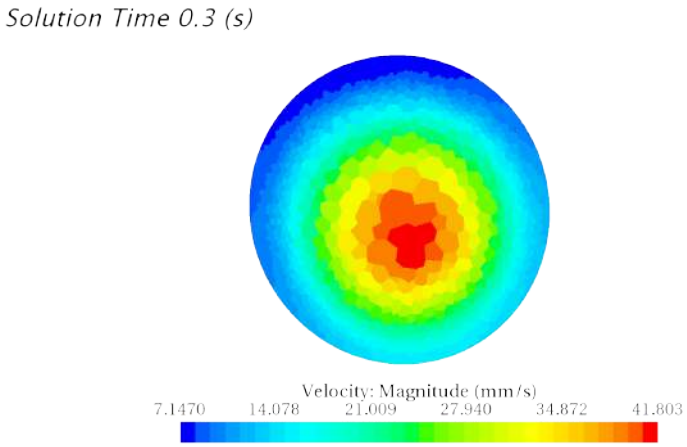

(b) Sectional cut A-A' of the velocity field in midsection of the aneurysm sac at t=0.3 s.

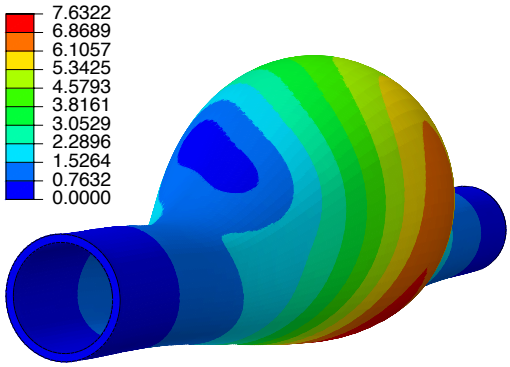

(c) Displacement field at $t = 0.3$ s in mm.

Figure 3.10: Results for $\beta = 0.2$ at pressure diastolic peak.

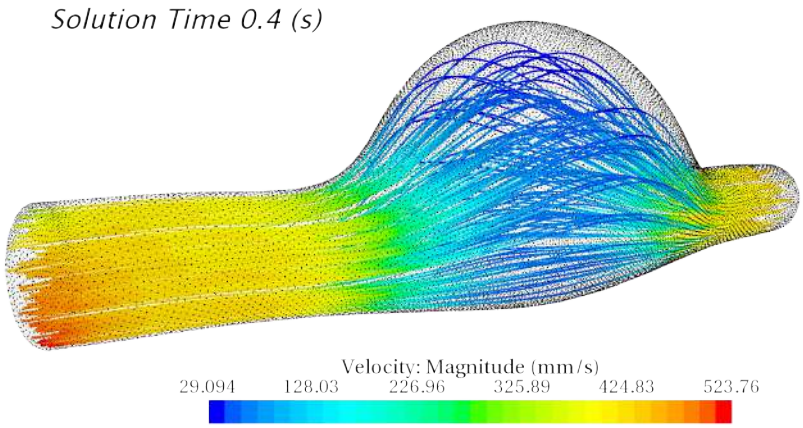

(a) Side view of velocity streamlines at t=0.4 s.

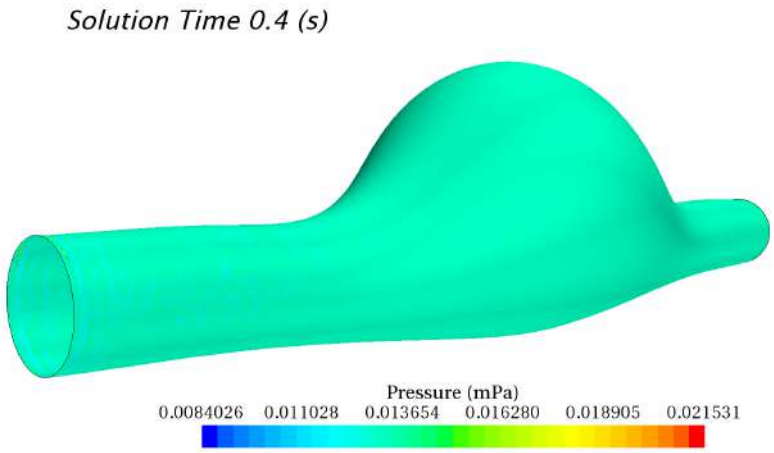

(b) Fluid pressure at the wall at t=0.4 s.

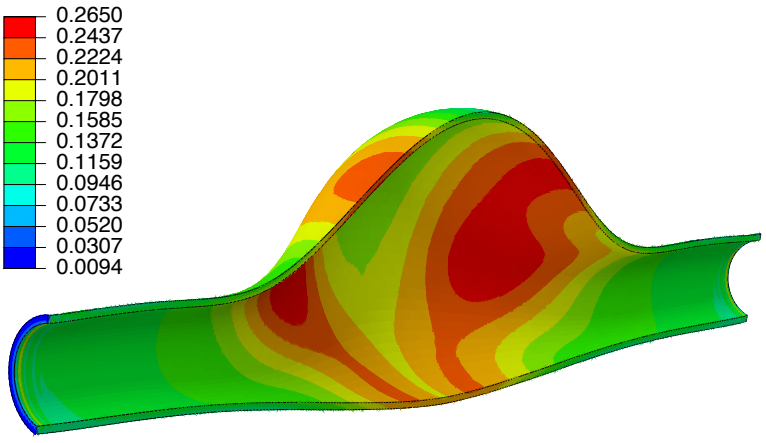

(c) Sagittal view of the Von Mises stress distribution at t=0.4 s, in MPa.

Figure 3.11: Wall stress results for $\beta = 0.2$ at velocity systolic peak.

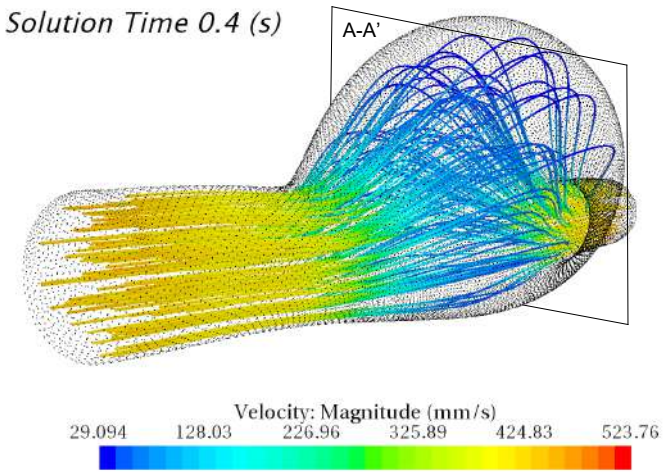

(a) Perspective view of the velocity streamlines at t=0.4 s. The sectional cut A-A' is depicted in the undeformed configuration of the sac.

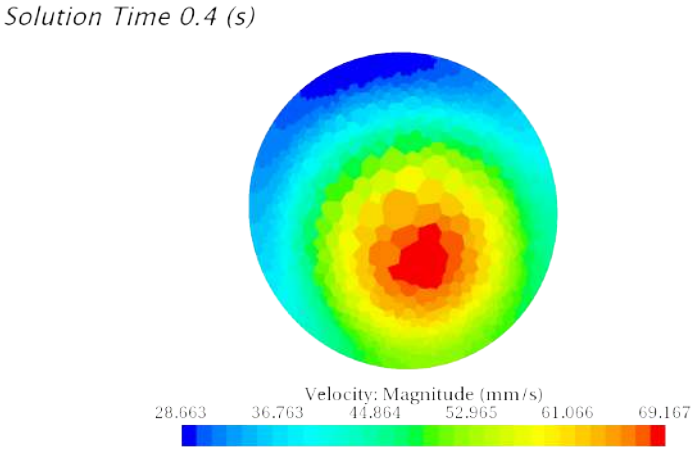

(b) Sectional cut A-A' of the velocity field in the midsection of the aneurysm sac at t=0.4 s.

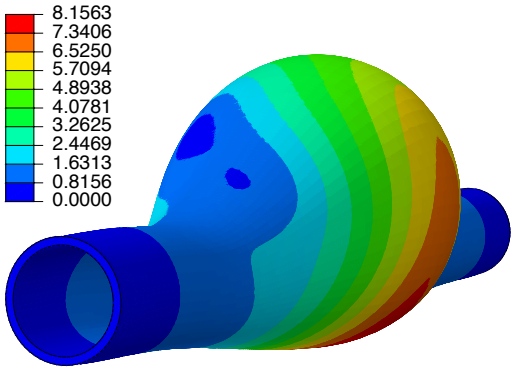

(c) Displacement field at $t = 0.4$ s in mm.

Figure 3.12: Displacement results for $\beta = 0.2$ at velocity systolic peak.

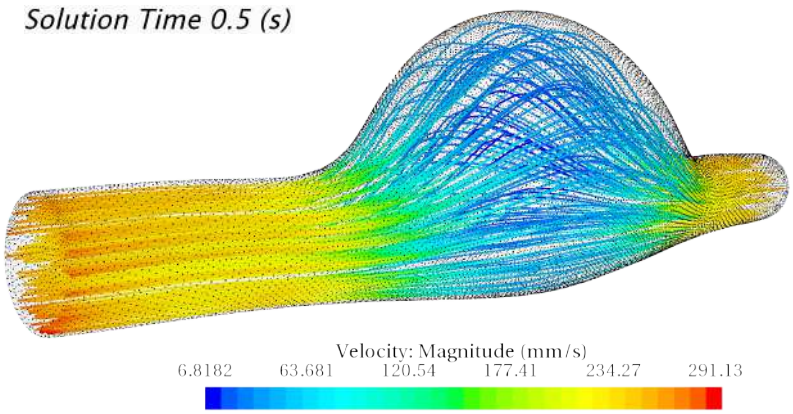

(a) Side view of velocity streamlines at t=0.5 s.

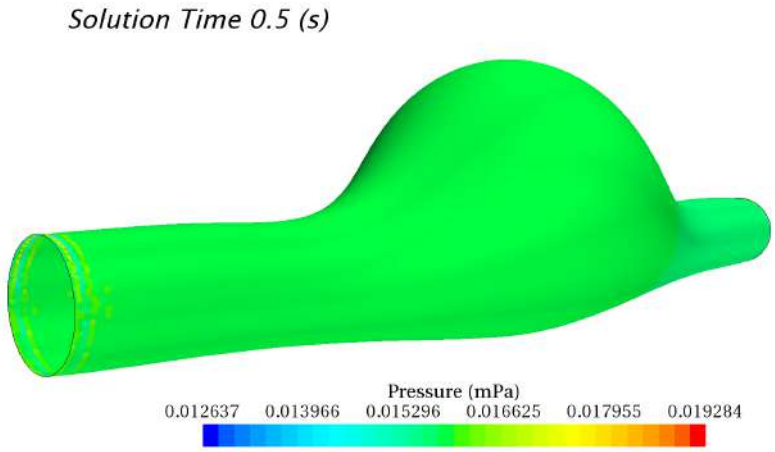

(b) Fluid pressure at the wall at t=0.5 s.

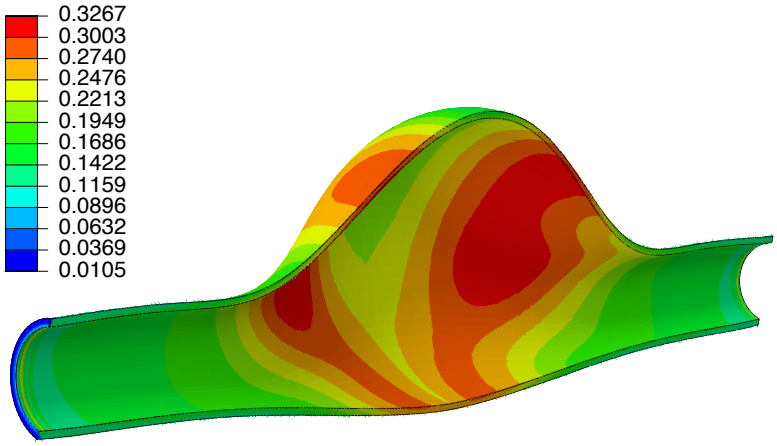

(c) Sagittal view of the Von Mises stress distribution at t=0.5 s, in MPa.

Figure 3.13: Wall stress results for $\beta = 0.2$ at pressure systolic peak.

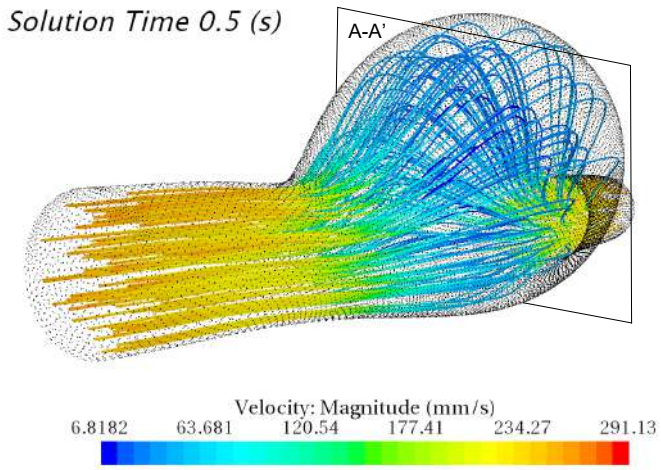

(a) Perspective view of the velocity streamlines at t=0.5 s. The sectional cut A-A' is depicted in the undeformed configuration of the sac.

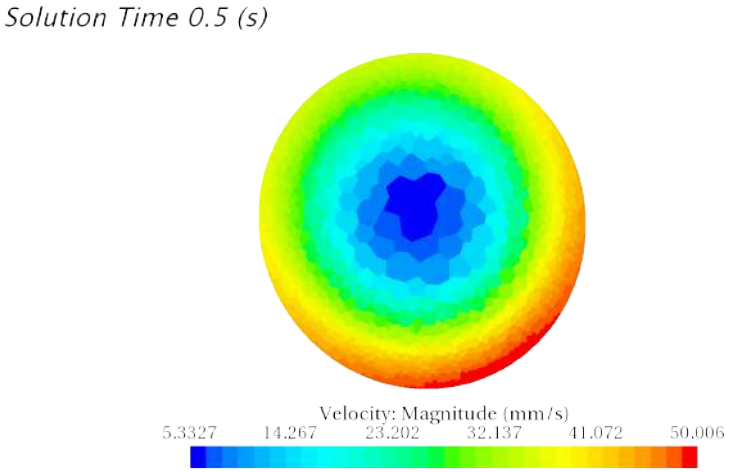

(b) Sectional cut A-A' of the velocity field in the midsection of the aneurysm sac at t=0.5 s.

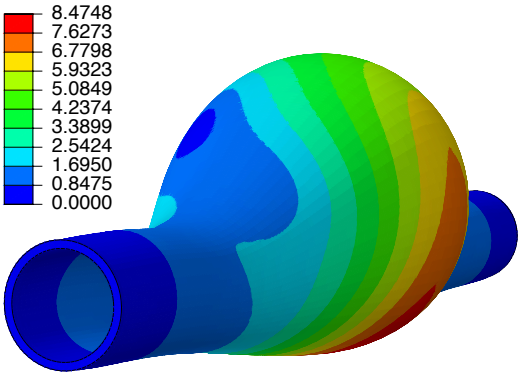

(c) Displacement field at $t = 0.5$ s in mm.

Figure 3.14: Displacement results for $\beta = 0.2$ at pressure systolic peak.

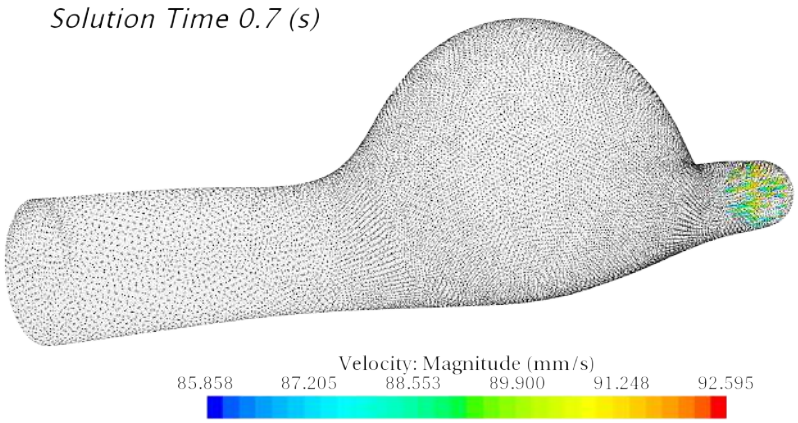

(a) Side view of velocity streamlines at t=0.7 s.

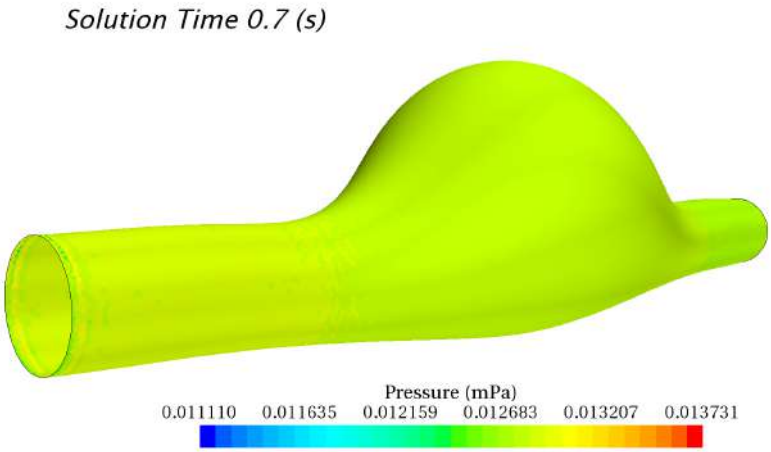

(b) Fluid pressure at the wall at t=0.7 s.

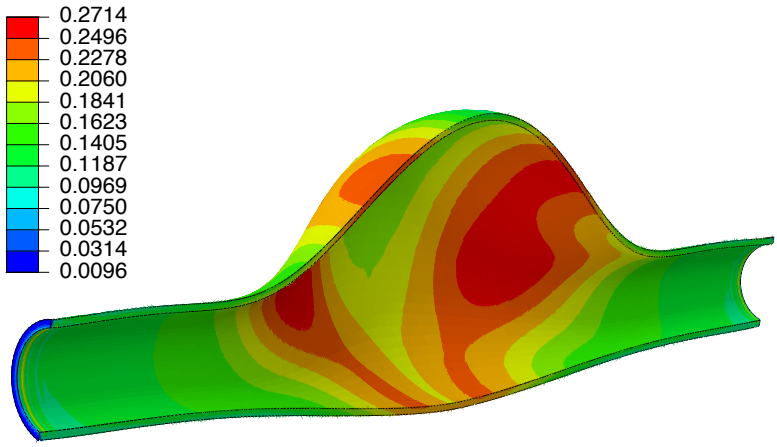

(c) Sagittal view of the Von Mises stress distribution at t=0.7 s, in MPa.

Figure 3.15: Wall stress results for $\beta = 0.2$ at velocity diastolic peak.

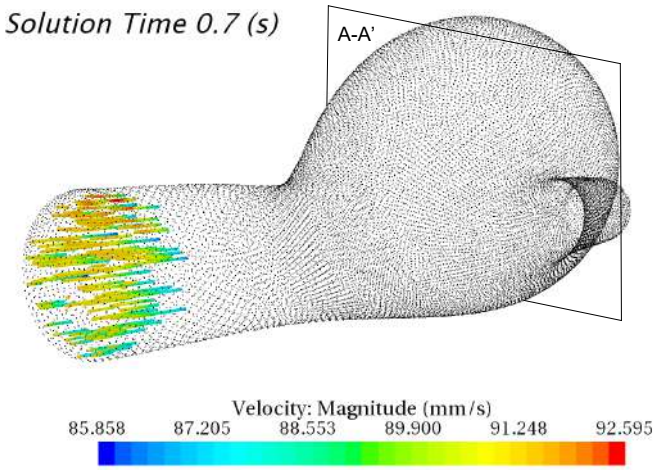

(a) Perspective view of the velocity streamlines at t=0.7 s. The sectional cut A-A' is depicted in the undeformed configuration of the sac.

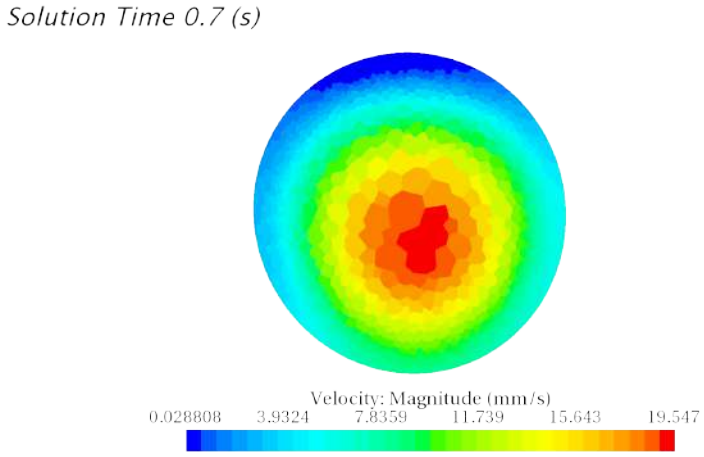

(b) Sectional cut A-A' of the velocity field in the midsection of the aneurysm sac at t=0.7 s.

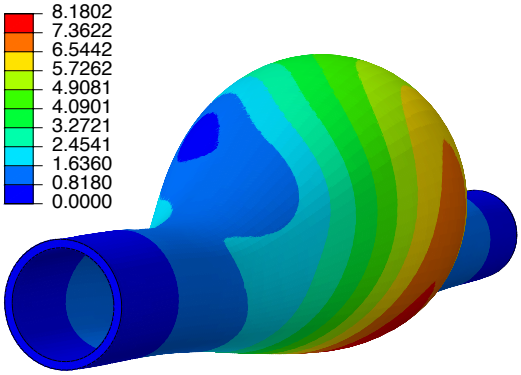

(c) Displacement field at $t = 0.7$ s in mm.

Figure 3.16: Displacement results for $\beta = 0.2$ at velocity diastolic peak.

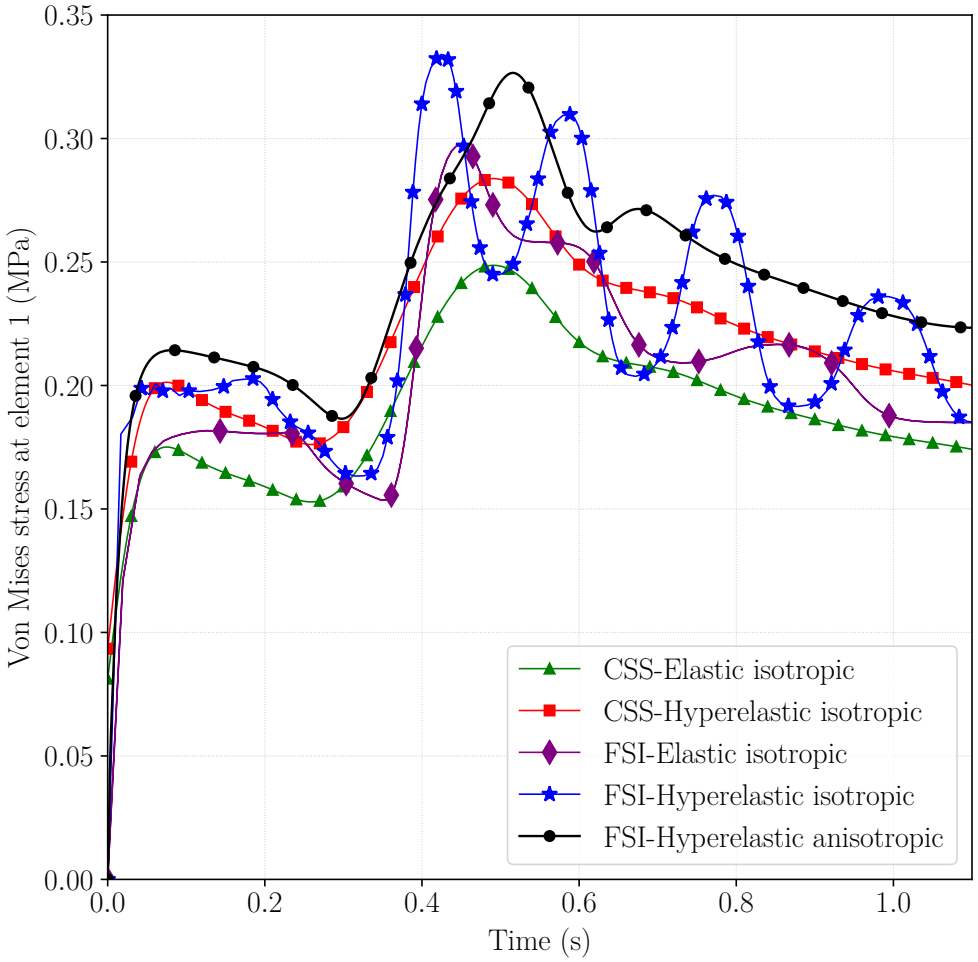

(a) Evolution of wall stresses during the cardiac cycle for different constitutive models and numerical techniques. The results of the CSS (Computational Solid Stress) and FSI (Fluid-Structure Interaction) models for the elastic and hyperelastic isotropic walls have been taken from [55].

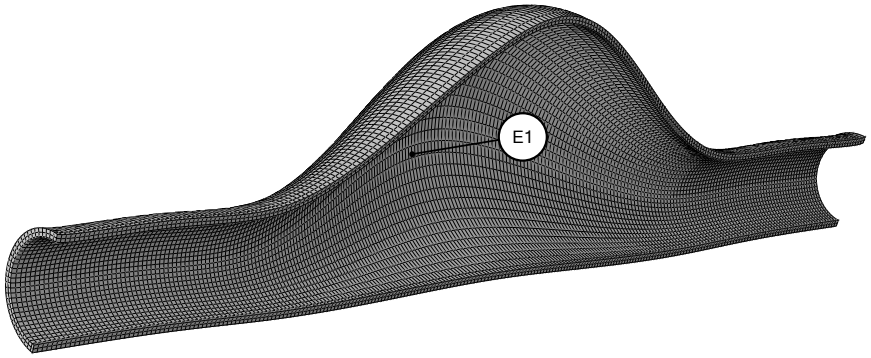

(b) Location of element 1 in the mesh.

Figure 3.17: Comparison of Von Mises wall stresses during a full cardiac cycle.

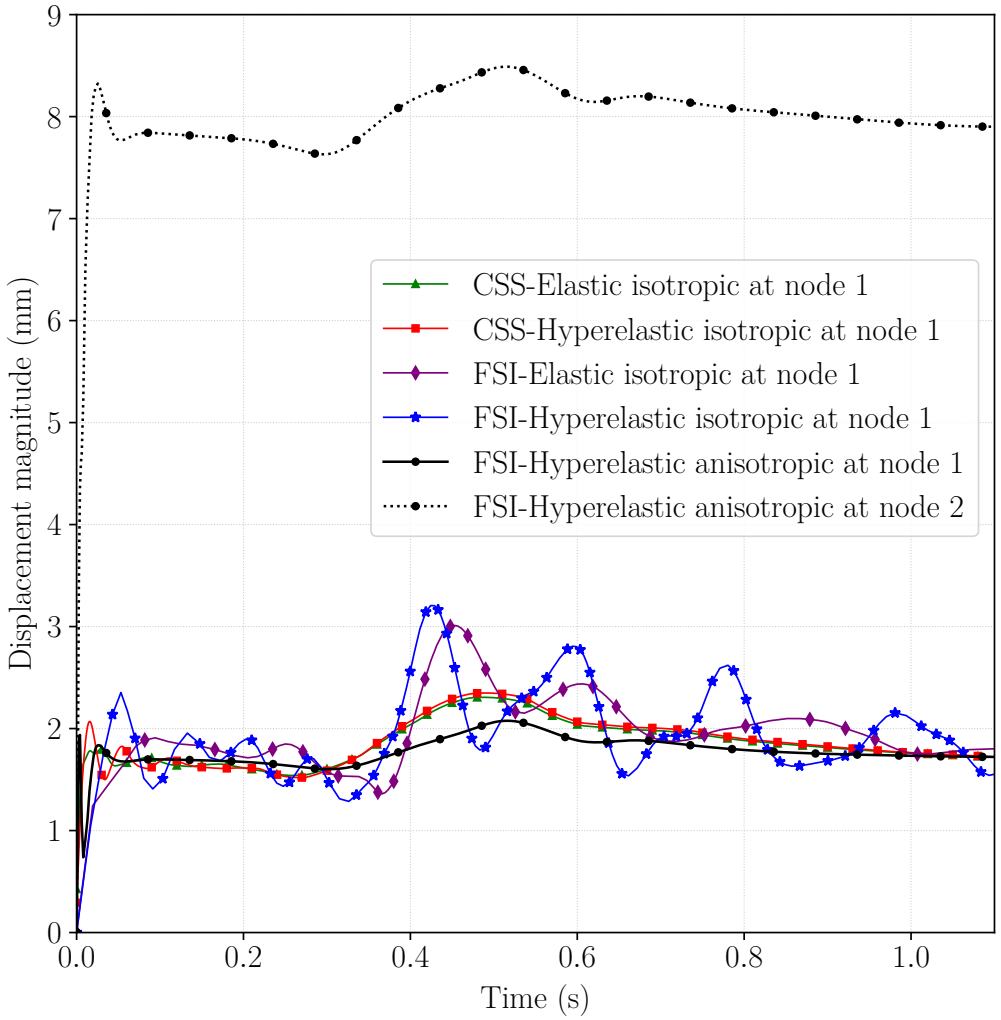

(a) Evolution of wall displacements during the cardiac cycle for different constitutive models and numerical techniques. The results of the CSS (Computational Solid Stress) and FSI (Fluid-Structure Interaction) models for the elastic and hyperelastic isotropic walls have been taken from [55].

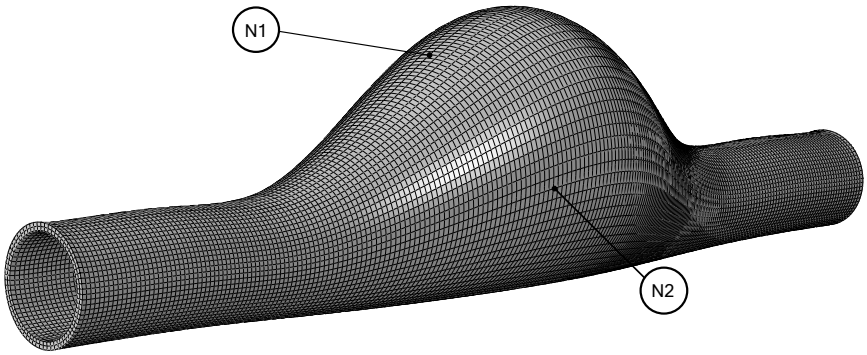

(b) Location of nodes 1 and 2 in the mesh.

Figure 3.18: Comparison of wall displacements during a full cardiac cycle.

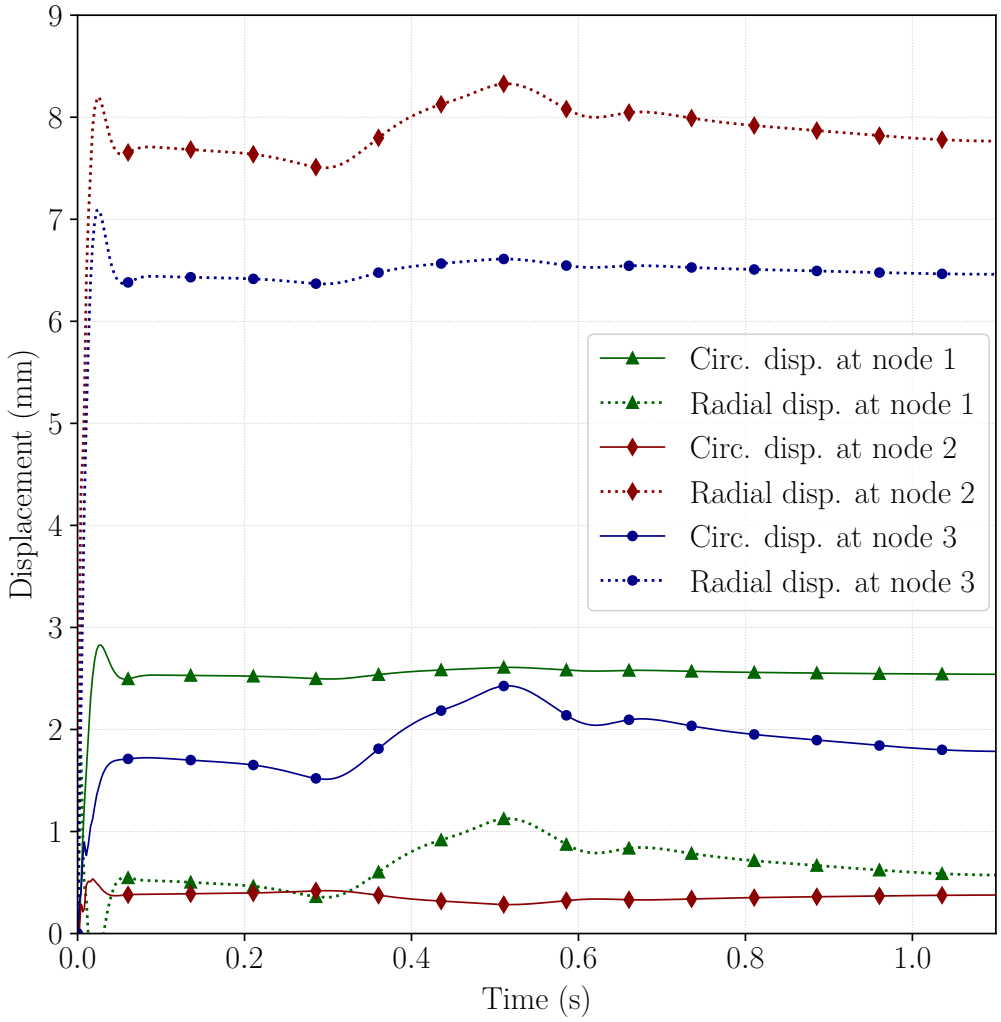

(a) Evolution of radial and circumferential wall displacements during the cardiac cycle for three different nodes in the FSI-Hyperelastic anisotropic model.

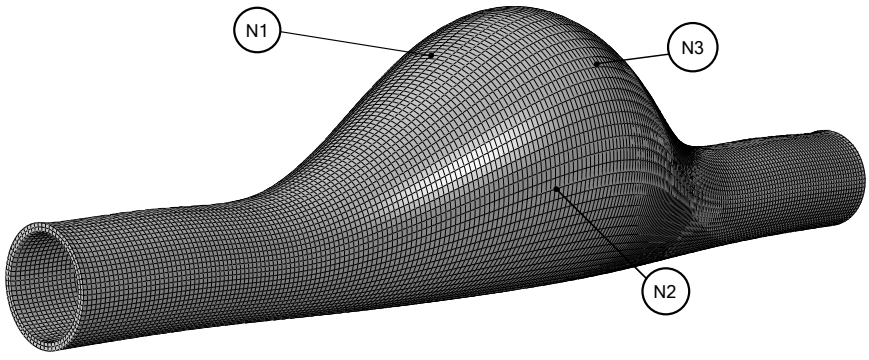

(b) Location of nodes 1, 2 and 3 in the mesh of the solid domain.

Figure 3.19: Evaluation of material anisotropy by analyzing radial and circumferential wall displacements during a full cardiac cycle.

4

Conclusions and future research

4.1 Conclusions

This investigation attempts to demonstrate the importance of considering the mechanical contribution of the three layers that make up aortic tissue during the development of intimal hyperplasia. To do this, finite element analyses were performed on three different idealized geometries of AAA models subjected to realistic loading conditions. These simulations were calibrated considering the structural response of the aneurysmal tissue through uniaxial tests of aorta strips cut in the circumferential and axial directions and plane strain human aorta rings under systolic blood pressure.

Resultant stresses and displacements were obtained for an intact (mono-layered) artery wall, which represents the mean structural response of the three-layer composite tissue, and a three-layered wall, in which each layer has been modeled separately with its own material properties using a continuum mesh, observing differences of about 30% concerning the stresses and a maximum of 53%, which decreased to 0.75% with the asymmetry, regarding the displacements. This comparison was also carried out with other studies performed on idealized AAA geometries with the same parameterization, but with different constitutive models. We found out maximum differences of 54% in terms of stresses and 48% in terms of displacements for an elastic isotropic mono-layered wall (EIM), and 51% and 14% for a hyperelastic isotropic mono-layer wall (HIM), with respect to a three-layered hyperelastic anisotropic wall (H3A).

Regarding the idealized geometry used, our results corroborate that the stress distribution is strongly dependent on the asymmetry of the sac, inasmuch as symmetric AAAs showed a uniform stress distribution around the sac, while the most asymmetric geometries presented noteworthy stress concentrations in the inflection points of the curvature of the sac, leading to greater peak wall stresses, and therefore higher rupture potential.

The obtained results show an early exponential stiffening of tunica intima that makes it definitely load-bearing when it becomes thickened because of intimal hyperplasia. This phenomena may be caused by two factors. The first one is the collagenization; The diffuse thickening of the innermost layer of the abdominal aorta has been associated by many studies with collagenization of the elastic and hyper-plastic layers, which, from the mechanical point of view, increases the

dispersion in the families of collagen fibers, governed by κ in the constitutive model used, and stiffens up the intimal layer. The second factor could be related to the proliferation of smooth muscle cells between the endothelium and the internal elastic lamina. In any case, the intimal layer shows the highest percentages of stress absorption.

Our results suggest that tunica intima may act as a stiffener when thickened due to hyperplasia, since it has a mean stress absorption ratio of 78%, while adventitia and media only absorb 7% and 11% of the total circumferential stress on the AAA, respectively. This fact points out the necessity of including tunica intima in multi-layered models of AAAS to obtain accurate peak wall stresses, and to improve the rupture risk assessment.

On the other hand, the consideration of shear forces through FSI simulations is important to account for non-symmetric stress and displacement distributions, which completely change the prediction of rupture. It has been demonstrated that the results obtained with Computational Solid Stress models (CSS) underestimate the FSI-predicted maximum values by 24% in terms of stresses, and 72% in terms of displacements. However, even taking into account shear stresses, mono-layered models are not enough accurate to capture the real mechanical behavior of aneurysmatic tissue, since three-layered models show higher peak wall stresses (0.64 vs 0.32 MPa) . Therefore, a FSI analysis of a three-layered aneurysm considering a hyperelastic anisotropic wall would be promising to warrant further investigation in this field.

4.2 Future research

In respect of future studies, first of all they must consider the implementation of residual stresses in the arterial modeling to get more realistic results, since residual stresses/stretches have been proved to produce a significant impact on the mechanical response of aortic tissue to external loads [13]. The dynamic mechanobiological processes are also important to take into account the evolution of lesion growth and remodeling of the wall properties. In this sense, growth and remodeling techniques (G&R) will be necessary to analyze how the mechanical environment influences the tissue's developing morphology. Last but not least, it is crucial to consider that, the existence of intraluminal thrombus (ILT) is associated with early rupture of abdominal aortic aneurysm. Therefore, future and more advanced CSS and FSI models must include ILT as an additional rupture risk factor.

Bibliography

[1] LeFevre, M. L. "Screening for abdominal aortic aneurysm: U.S. Preventive Services Task Force recommendation statement." *Annals of internal medicine* 161.4 (2014), pp. 281–290.

[2] Kühnl, A., Erk, A., Trenner, M., Salvermoser, M., Schmid, V., and Eckstein, H.-H. "Incidence, Treatment and Mortality in Patients with Abdominal Aortic Aneurysms: An Analysis of Hospital Discharge Data from 2005–2014". *Deutsches Ärzteblatt International* 114.22-23 (2017), pp. 391–398.

[3] Lederle, F. A., Wilson, S. E., Johnson, G. R., Reinke, D. B., Littooy, F. N., Acher, C. W., Ballard, D. J., Messina, L. M., Gordon, I. L., Chute, E. P., Krupski, W. C., Busuttil, S. J., Barone, G. W., Sparks, S., Graham, L. M., Rapp, J. H., Makaroun, M. S., Moneta, G. L., Cambria, R. A., Makhoul, R. G., Eton, D., Ansel, H. J., Freischlag, J. A., and Bandyk, D. "Immediate repair compared with surveillance of small abdominal aortic aneurysms." *The New England journal of medicine* 346.19 (2002), pp. 1437–1444.

[4] Hans, S. S., Jareunpoon, O., Balasubramaniam, M., and Zelenock, G. B. "Size and location of thrombus in intact and ruptured abdominal aortic aneurysms". *Journal of Vascular Surgery* 41.4 (2005), pp. 584–588.

[5] Grootenboer, N., Bosch, J. L., Hendriks, J. M., and Sambeek, M. R. H. M. van. *Epidemiology, Aetiology, Risk of Rupture and Treatment of Abdominal Aortic Aneurysms: Does Sex Matter?* 2009.

[6] Rodríguez, J. F., Martufi, G., Doblaré, M., and Finol, E. A. "The effect of material model formulation in the stress analysis of abdominal aortic aneurysms". *Annals of biomedical engineering* 37.11 (2009), p. 2218.

[7] Vorp, D. A., Raghavan, M., and Webster, M. W. "Mechanical wall stress in abdominal aortic aneurysm: Influence of diameter and asymmetry". *Journal of Vascular Surgery* 27.4 (1998), pp. 632–639.

[8] Raghavan, M. L., Webster, M. W., and Vorp, D. A. "Ex vivo biomechanical behavior of abdominal aortic aneurysm: assessment using a new mathematical model." *Annals of biomedical engineering* 24.5 (1996), pp. 573–582.

[9] Movat, H. Z., More, R. H., and Haust, M. D. “The Diffuse Intimal Thickening of the Human Aorta with Aging”. *The American Journal of Pathology* 34.6 (1958), pp. 1023–1031.

[10] Glagov, S. and Zarins, C. K. “Is intimal hyperplasia an adaptive response or a pathologic process? Observations on the nature of nonatherosclerotic intimal thickening”. *Journal of Vascular Surgery* 10.5 (1989), pp. 571–573.

[11] Gasser, T. C., Ogden, R. W., and Holzapfel, G. A. “Hyperelastic modelling of arterial layers with distributed collagen fibre orientations”. *Journal of The Royal Society Interface* 3.6 (2006), pp. 15–35.

[12] Weisbecker, H., Pierce, D. M., Regitnig, P., and Holzapfel, G. A. “Layer-specific damage experiments and modeling of human thoracic and abdominal aortas with non-atherosclerotic intimal thickening”. *Journal of the Mechanical Behavior of Biomedical Materials* 12 (2012), pp. 93–106.

[13] Alastrué, V., Peña, E., Martínez, M. Á., and Doblaré, M. “Assessing the Use of the "Opening Angle Method" to Enforce Residual Stresses in Patient-Specific Arteries”. *Annals of Biomedical Engineering* 35.10 (2007), pp. 1821–1837.

[14] Scotti, C. M., Shkolnik, A. D., Muluk, S. C., and Finol, E. a. “Fluid-structure interaction in abdominal aortic aneurysms: effects of asymmetry and wall thickness”. *BioMedical Engineering Online* 4.1 (2005), p. 64.

[15] Raghavan, M. L. and Vorp, D. A. “Toward a biomechanical tool to evaluate rupture potential of abdominal aortic aneurysm: identification of a finite strain constitutive model and evaluation of its applicability”. *Journal of Biomechanics* 33.4 (2000), pp. 475–482.

[16] Xenos, M., Rambhia, S. H., Alemu, Y., Einav, S., Labropoulos, N., Tassiopoulos, A., Ricotta, J. J., and Bluestein, D. “Patient-Based Abdominal Aortic Aneurysm Rupture Risk Prediction with Fluid Structure Interaction Modeling”. *Annals of Biomedical Engineering* 38.11 (2010), pp. 3323–3337.

[17] Rodríguez, J. F., Ruiz, C., Doblaré, M., and Holzapfel, G. A. “Mechanical Stresses in Abdominal Aortic Aneurysms: Influence of Diameter, Asymmetry, and Material Anisotropy”. *Journal of Biomechanical Engineering* 130.2 (2008), p. 021023.

[18] Joldes, G. R., Miller, K., Wittek, A., and Doyle, B. “A simple, effective and clinically applicable method to compute abdominal aortic aneurysm wall stress”. *Journal of the Mechanical Behavior of Biomedical Materials* 58 (2016), pp. 139–148.

[19] Ahamed, T., Dorfmann, L., and Ogden, R. “Modelling of residually stressed materials with application to AAA”. *Journal of the Mechanical Behavior of Biomedical Materials* 61 (2016), pp. 221–234.

[20] Labrosse, M. R., Gerson, E. R., Veinot, J. P., and Beller, C. J. “Mechanical characterization of human aortas from pressurization testing and a paradigm shift for circumferential residual stress”. *Journal of the Mechanical Behavior of Biomedical Materials* 17 (2013), pp. 44–55.

[21] Gao, F., Watanabe, M., and Matsuzawa, T. "Stress analysis in a layered aortic arch model under pulsatile blood flow". *Biomedical engineering online* 5 (2006), pp. 25–25.

[22] Gao, F., Ohta, O., and Matsuzawa, T. "Fluid-structure interaction in layered aortic arch aneurysm model: assessing the combined influence of arch aneurysm and wall stiffness". *Australasian Physics & Engineering Sciences in Medicine* 31.1 (2008), p. 32.

[23] Gao, F., Ueda, H., Gang, L., and Okada, H. "Fluid structure interaction simulation in three-layered aortic aneurysm model under pulsatile flow: Comparison of wrapping and stenting". *Journal of Biomechanics* 46.7 (2013), pp. 1335–1342.

[24] Simsek, F. G. and Kwon, Y. W. "Investigation of material modeling in fluid-structure interaction analysis of an idealized three-layered abdominal aorta: aneurysm initiation and fully developed aneurysms". *Journal of biological physics* 41.2 (2015), pp. 173–201.

[25] Gholipour, A., Ghayesh, M. H., Zander, A., and Mahajan, R. "Three-dimensional biomechanics of coronary arteries". *International Journal of Engineering Science* 130 (2018), pp. 93–114.

[26] Pierce, D. M., Fastl, T. E., Rodríguez-Vila, B., Verbrugghe, P., Fourneau, I., Maleux, G., Herijgers, P., Gomez, E. J., and Holzapfel, G. A. "A method for incorporating three-dimensional residual stretches/stresses into patient-specific finite element simulations of arteries". *Journal of the Mechanical Behavior of Biomedical Materials* 47 (2015), pp. 147–164.

[27] Strbac, V., Pierce, D., Rodríguez-Vila, B., Sloten, J. V., and Famaey, N. "Rupture risk in abdominal aortic aneurysms: A realistic assessment of the explicit GPU approach". *Journal of Biomechanics* 56 (2017), pp. 1–9.

[28] Mills, C. J., Gabe, I. T., Gault, J. H., Mason, D. T., Ross, J., Braunwald, E., and Shillingford, J. P. "Pressure-flow relationships and vascular impedance in man". *Cardiovascular Research* 4.4 (1970), pp. 405–417.

[29] Martino, E. D., Guadagni, G., Fumero, A., Ballerini, G., Spirito, R., Biglioli, P., and Redaelli, A. "Fluid–structure interaction within realistic three-dimensional models of the aneurysmatic aorta as a guidance to assess the risk of rupture of the aneurysm". *Medical Engineering & Physics* 23.9 (2001), pp. 647–655.

[30] Li, Z. and Kleinstreuer, C. "A comparison between different asymmetric abdominal aortic aneurysm morphologies employing computational fluid–structure interaction analysis". *European Journal of Mechanics - B/Fluids* 26.5 (2007), pp. 615–631.

[31] Georgakarakos, E., Ioannou, C., Kamarianakis, Y., Papaharilaou, Y., Kostas, T., Manousaki, E., and Katsamouris, A. "The Role of Geometric Parameters in the Prediction of Abdominal Aortic Aneurysm Wall Stress". *European Journal of Vascular and Endovascular Surgery* 39.1 (2010), pp. 42–48.

[32] Wang, X. and Li, X. "Computational simulation of aortic aneurysm using FSI method: Influence of blood viscosity on aneurismal dynamic behaviors". *Computers in Biology and Medicine* 41.9 (2011), pp. 812–821.

[33] Raghavan, M., Vorp, D. A., Federle, M. P., Makaroun, M. S., and Webster, M. W. "Wall stress distribution on three-dimensionally reconstructed models of human abdominal aortic aneurysm". *Journal of Vascular Surgery* 31.4 (2000), pp. 760–769.

[34] Wang, D. H., Makaroun, M. S., Webster, M. W., and Vorp, D. A. "Effect of intraluminal thrombus on wall stress in patient-specific models of abdominal aortic aneurysm". *Journal of Vascular Surgery* 36.3 (2002), pp. 598–604.

[35] Chandra, S., Raut, S. S., Jana, A., Biederman, R. W., Doyle, M., Muluk, S. C., and Finol, E. A. "Fluid-Structure Interaction Modeling of Abdominal Aortic Aneurysms: The Impact of Patient-Specific Inflow Conditions and Fluid/Solid Coupling". *Journal of Biomechanical Engineering* 135.8 (2013), pp. 081001–081001-14.

[36] Li, Z.-Y., U-King-Im, J., Tang, T. Y., Soh, E., See, T. C., and Gillard, J. H. "Impact of calcification and intraluminal thrombus on the computed wall stresses of abdominal aortic aneurysm". *Journal of Vascular Surgery* 47.5 (2008), pp. 928–935.

[37] Maier, A., Gee, M. W., Reeps, C., Eckstein, H.-H., and Wall, W. A. "Impact of calcifications on patient-specific wall stress analysis of abdominal aortic aneurysms". *Biomechanics and Modeling in Mechanobiology* 9.5 (2010), pp. 511–521.

[38] Geest, J. P. V., Sacks, M. S., and Vorp, D. A. "The effects of aneurysm on the biaxial mechanical behavior of human abdominal aorta". *Journal of Biomechanics* 39.7 (2006), pp. 1324–1334.

[39] Vito, R. P. and Hickey, J. "The mechanical properties of soft tissues—II: The elastic response of arterial segments". *Journal of Biomechanics* 13.11 (1980), pp. 951–957.

[40] Holzapfel, G. A., Gasser, T. C., and Ogden, R. W. "A New Constitutive Framework for Arterial Wall Mechanics and a Comparative Study of Material Models". *Journal of elasticity and the physical science of solids* 61.1 (2000), pp. 1–48.

[41] Schriefl, A. J., Zeindlinger, G., Pierce, D. M., Regitnig, P., and Holzapfel, G. A. "Determination of the layer-specific distributed collagen fibre orientations in human thoracic and abdominal aortas and common iliac arteries". *Journal of The Royal Society Interface* 9.71 (2012), pp. 1275–1286.

[42] *ABAQUS 6.14 Documentation*. Dassault Systèmes. 2014.

[43] Holzapfel, G. A., Sommer, G., and Regitnig, P. "Anisotropic Mechanical Properties of Tissue Components in Human Atherosclerotic Plaques". *Journal of Biomechanical Engineering* 126.5 (2004), pp. 657–665.

[44] Holzapfel, G. A., Sommer, G., Gasser, C. T., and Regitnig, P. "Determination of layer-specific mechanical properties of human coronary arteries with nonatherosclerotic intimal thickening and related constitutive modeling". *American Journal of Physiology-Heart and Circulatory Physiology* 289.5 (2005), H2048–H2058.

[45] Díaz, J. *Aneupy. A Python code for parametric generation of abdominal aortic aneurysms.* `http://github.com/jacobo-diaz/aneupy`. Universidade da Coruña, 2016.

[46] *SALOME 7.5.1. The open source integration platform for numerical simulation.* 2015.

[47] Galland, R., Whiteley, M., and Magee, T. "The fate of patients undergoing surveillance of small abdominal aortic aneurysms". *European Journal of Vascular and Endovascular Surgery* 16.2 (1998), pp. 104–109.

[48] Raghavan, M. L., Kratzberg, J., Castro de Tolosa, E. M. M., Hanaoka, M. M., Walker, P., Silva, E. S. da, and Tolosa, E. de. "Regional distribution of wall thickness and failure properties of human abdominal aortic aneurysm." *Journal of biomechanics* 39.16 (2006), pp. 3010–3016.

[49] Raghavan, M. L., Hanaoka, M. M., Kratzberg, J. A., Higuchi, M. d. L., and Silva, E. S. da. "Biomechanical failure properties and microstructural content of ruptured and unruptured abdominal aortic aneurysms". *Journal of Biomechanics* 44.13 (2011), pp. 2501–2507.

[50] Scotti, C. M., Jimenez, J., Muluk, S. C., and Finol, E. A. "Wall stress and flow dynamics in abdominal aortic aneurysms: finite element analysis vs. fluid–structure interaction". *Computer Methods in Biomechanics and Biomedical Engineering* 11.3 (2008), pp. 301–322.

[51] Bazilevs, Y., Alamo, J. C. del, and Humphrey, J. D. "From imaging to prediction: Emerging non-invasive methods in pediatric cardiology". *Progress in Pediatric Cardiology* 30.1-2 (2010), pp. 81–89.

[52] *STAR CCM+ Documentation.* Siemens PLM Software. 2018.

[53] Sillem, A. "Feasibility study of a tire hydroplaning simulation in a monolithic finite element code using a coupled Eulerian-Lagrangian method". MA thesis. Faculty of electrical engineering, mathematics and computer science. Delft institute of applied mathematics., 2008.

[54] Sieber., G. "Numerical Simulation of Fluid-Structure Interaction Using Loose Coupling Methods". PhD thesis. Vom Fachbereich Maschinenbau an der Technischen Universität Darmstadt., 2002.

[55] Fernández García, M. and Romera Rodríguez Jacobo Díaz García, L. E. "Stress-strain analysis of abdominal aortic aneurysms considering the fluid structure-interaction". *Universidade da Coruña* (2016).

[56] Donea, J., Huerta, A., Ponthot, J.-P., and Rodríguez-Ferran, A. "Arbitrary Lagrangian-Eulerian Methods". *Encyclopedia of Computational Mechanics* (2004), pp. 413–437.

[57] Milnor, W. *Hemodynamics.* Baltimore: Williams and Wilkins, 1989.

[58] Fournier, R. *Basic transport phenomena in biomedical engineering*. Philadelphia: Taylor & Francis, 1998.

[59] Finol, E. A., Keyhani, K., and Amon, C. H. "The Effect of Asymmetry in Abdominal Aortic Aneurysms Under Physiologically Realistic Pulsatile Flow Conditions". *Journal of Biomechanical Engineering* 125.2 (2003), p. 207.

[60] Hilber, H. M., Hughes, T. J. R., and Taylor, R. L. "Improved numerical dissipation for time integration algorithms in structural dynamics". *Earthquake Engineering & Structural Dynamics* 5.3 (1977), pp. 283–292.